An improved phase-field algorithm for simulating the impact of a drop on a substrate in the presence of surfactants

Chenxi Wang [a,b], Ming-Chih Lai [c], Zhen Zhang [d,a,*]

[a] *Shenzhen International Center for Mathematics, Southern University of Science and Technology (SUSTech), Shenzhen 518055, PR China*

[b] *Department of Mathematics, Harbin Institute of Technology, Harbin 150001, PR China*

[c] *Department of Applied Mathematics, National Yang Ming Chiao Tung University, 1001, Ta Hsueh Road, Hsinchu 300, Taiwan*

[d] *Department of Mathematics, National Center for Applied Mathematics (Shenzhen), Southern University of Science and Technology (SUSTech), Shenzhen 518055, PR China*

A R T I C L E   I N F O

A B S T R A C T

This paper is devoted to the numerical study of droplet impact on solid substrates in the presence of surfactants. We formulate the problem in an energetically variational framework and introduce an incompressible Cahn-Hilliard-Navier-Stokes system for the phase-field modeling of two-phase flows. Flory-Huggins potential and generalized Navier boundary condition are used to account for soluble surfactants and moving contact lines. Based on the convex splitting and pressure stabilization technique, we develop unconditionally energy stable schemes for this model. The discrete energy dissipation law for the original energy is rigorously proved for the first-order scheme. The numerical methods are implemented using finite difference method in three-dimensional cylindrical coordinates with axisymmetry. Using the proposed methods for this model, we systematically study the impact dynamics of both clean and contaminated droplets (with surfactants) in a series of numerical experiments. In general, the dissipation in the impact dynamics of a contaminated drop is smaller than that in the clean case, and topological changes are more likely to occur for contaminated drops. Adding surfactants can significantly influence the impact phenomena, leading to the enhancement of adherence effect on hydrophilic surfaces and splashing on hydrophobic surfaces. Some qualitative agreements with experiments are also obtained.

1. Introduction

The effect of surfactants, namely surface-active substances, has been the subject of intense study for a long time and is of great interest in many industrial applications. Surfactants can be used as emulsifiers, cleaning detergents, foaming agents, wetting agents, and dispersants [1–3]. Recently, surfactants have been widely used in microsystems with the presence of interfaces, where the capillary effect dominates the inertia of fluids [4]. An important application is surfactant-based inkjet printing, in which surfactants can help the adsorption of ink onto hydrophobic surfaces [5]. The presence of surfactants in multiphase flow has great effects on the dynamics of interface by altering the interfacial tension. In addition, when surfactants are not uniformly distributed on the interface, the dynamical behavior of interface would also be significantly affected due to Marangoni effect [6]. These complex dynamics bring
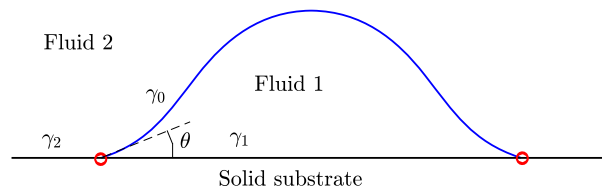
Fig. 1. A fluid-fluid interface intersects a solid substrate. The contact line (points) is represented by the red points; γ_0, γ_1 and γ_2 are respectively the surface tensions of the fluid-fluid interface and the two fluid-solid interfaces; θ is the contact angle. In equilibrium, the static contact angle θ_s satisfies the Young-Dupré equation $\gamma_0 \cos \theta_s = \gamma_2 - \gamma_1$. (For interpretation of the colors in the figure(s), the reader is referred to the web version of this article.)

difficulty to experimental study of multiphase flow with surfactants. As an alternative, modeling and numerical simulations have played an increasingly significant role, although there remain challenging tasks.

For decades, modeling and numerical simulations of surfactant-driven hydrodynamics have attracted much attention. The surfactant transport model was first presented by [7] and then revised in [8] by introducing convection-diffusion system on surface. Based on this model, many numerical methods have been developed to simulate multiphase flow with surfactants. These include front tracking method [9], level-set method [10], volume-of-fluid method [11], immersed boundary/immersed interface method [12], phase-field method [13,14], and lattice Boltzmann method [15]. Among these methods, the phase-field method is of particular interests due to its versatility in modeling as well as simulations. In phase-field models, an order parameter is introduced to label the two different phases with different values, and the sharp interface is diffused and represented by a smooth function. The phase-field method was first used to study interfacial dynamics with surfactants in [16], resulting in the phase-field surfactant (PFS) model, where two order parameters were introduced to represent local volume fraction of one phase (usually called phase-field variable) and surfactant concentration respectively. Numerous works have shown great performance of the PFS model in simulations of multiphase systems with surfactants [17–19]. Recently, the PFS models were extensively investigated in the presence of hydrodynamics [14,20]. In these models, besides the classical Ginzburg-Landau free energy potential, the Flory-Huggins potential with logarithmic terms is typically inserted into the total free energy in order to model mixing entropy due to the addition of surfactants. Moreover, a nonlinearly coupled term in both phase-field variable and surfactant concentration is present to account for the adsorption of surfactants on the fluid interface [21,22].

As long as a total free energy is given, a phase-field model can be derived as a gradient flow system which satisfies energy dissipation law. For numerical methods of such systems, energy stability is one of the most important properties that need to be take care of [23]. The stiffness arising from nonlinear terms in the free energy also makes it difficult to design efficient numerical schemes with large time steps. A number of techniques have been developed for the construction of energy stable schemes. Using convex splitting approach, unconditionally energy stable methods for the Cahn-Hilliard equation were developed by [24]. The major idea is to implicitly treat the convex terms of energy functional and explicitly treat the concave terms. This technique was successfully applied to numerically solve the PFS model [18]. In a similar manner, the so-called stabilization method was proposed by introducing a stabilization term to avoid solving nonlinear system [25]. Despite high efficiency and easy-to-implement, these two methods are not easily employed in developing high-order schemes with unconditional energy stability. Recently, by generalizing the Lagrange multiplier method [26], [27] proposed an invariant energy quadratization (IEQ) approach with an auxiliary function representing the square root of the nonlinear part in the free energy. The original system is then transformed into an equivalent one with quadratized free energy, for which unconditionally energy stable and high-order linear decoupled schemes can be easily obtained. When a scalar auxiliary variable (SAV) is used instead of an auxiliary function, one can immediately obtain SAV approach which was first introduced by [28] and is more efficient. Since their births, the IEQ and SAV approaches have attracted great interest and have been applied in constructing high-order schemes for many dissipative systems, including the Cahn-Hilliard-Navier-Stokes (CHNS) model [29], the PFS model [30,19,31] and other systems [32,14,20,33,34]. It is worth mentioning that the IEQ/SAV approach is provable to be energy stable with respect to the modified energy instead of the original energy, which limits its use in physical systems sensitive to energy changes. Some other widely used energy stable methods also exist, for instance, fully implicit schemes and exponential time-differencing schemes [35,36].

When two immiscible fluids interacts with a solid substrate, a contact line forms as the intersection of fluid-fluid interface with the solid boundary. In equilibrium, the angle between the two interfaces, also known as contact angle, is related to the surface tensions of the three interfaces and determined by Young-Dupré equation [37] (Fig. 1). If one fluid is displaced by the other along the substrate, moving contact line (MCL) must be considered. As is well known, the incompatibility of the MCL with the conventional no-slip boundary condition emerges in continuum hydrodynamics, since non-integrable stress singularity is generated at the contact line due to the use of no-slip boundary condition. In the past decades, a number of approaches were proposed to resolve MCL problems by using hydrodynamic models, molecular dynamic models, and diffuse-interface models [38–44]. Recent modeling and simulation studies showed that the presence of surfactants can further influence contact line dynamics by changing fluid-fluid interfacial tension, leading to more complicated multiphase hydrodynamics [45–52]. This makes surfactants appealing in the processes of spray coating, wetting, and many biological applications [53].

Recent experiments indicated that surfactants play a very important role in controlling droplet impact dynamics [54,55], which is worth extensive study due to its potential applications in inkjet printing. The purpose of the present work is to develop a computational model that can be applied to systematically investigate surfactant-induced droplet impact on solid substrates. We aim to develop efficient numerical methods which are not only stable when using large time steps but also thermodynamically consis-

tent with the physical model. Among those models for multiphase flows with moving contact lines, diffuse interface models with generalized Navier boundary condition (GNBC) are of particular interests since they can easily handle topological changes during impact processes while being energetically variational [39,56]. By taking into accounts the surfactant transport, the incompressible two-phase flow and the MCL dynamics, we model the droplet impact process by the binary fluid phase-field surfactant system with moving contact lines (NS-PFS-MCL). This model allows for variable density and viscosity and was shown to yield energy dissipation law in a variational framework [49]. By using the convex splitting technique and the pressure stabilization method [57], we propose unconditionally energy stable schemes for the numerical discretization of the NS-PFS-MCL system. Different from previous works [14,19,20,30,31,50], we show that the proposed scheme satisfies the discrete energy law without modifying the original free energy. The proposed schemes are efficiently implemented in three-dimensional axisymmetric cylindrical coordinates and applied to the numerical study of droplet impact on solid substrates with satisfactory accuracy.

Another contribution of the paper is to systematically investigate the effect of surfactants on droplet impact dynamics on solid substrates, which is highly demanded in numerical works. Specifically, different impact phenomena, such as adherence, bouncing/partial bouncing and splashing, are numerically compared and analyzed from the viewpoint of dissipations for both clean and contaminated (by surfactants) droplets. Following the experimental and numerical works on impact dynamics of clean droplets [58–61], we choose typical dimensionless parameters (the Reynolds number, the Weber number and the wettability of solid surface) in our numerical simulations, giving rise to seven representative examples for demonstration of the surfactant effect on modifying impact dynamics. The overall effect of surfactants is to make the droplet more hydrophilic/hydrophobic on hydrophilic/hydrophobic surfaces: adding surfactants into an impact droplet can strengthen the adherence effect on hydrophilic surfaces (demonstrated in Example 7); the presence of surfactants makes a splashing droplet break up into more small drops on hydrophobic surfaces (shown in Example 5). In general, the dissipation in the impact dynamics of a contaminated drop is smaller than that in the clean case, and topological changes are more likely to occur for contaminated drops. Moreover, adding surfactants may induce some qualitative changes in droplet impact phenomena. A clean adherent droplet could experience complete bouncing when surfactants are added (Example 2); a clean droplet which completely rebounds becomes partially bounced in the presence of surfactants (Example 3). Last but not least, we obtain qualitative agreements with experimental results for impact dynamics in the case without surfactants [59], and simulate impact processes for contaminated drops as comparisons.

The rest of this paper is organized as follows. In Sect. 2, we introduce the binary fluid PFS model with MCL and describe its energy dissipation law. In Sect. 3, the semi-discrete schemes are proposed, and the energy stability property is proved for the first-order scheme. An efficient numerical implementation are also discussed. The accuracy test and discrete energy law are numerically validated in Sect. 4. We also present extensive numerical experiments to demonstrate the effect of surfactants on hydrodynamics with moving contact lines. In particular, droplet impact dynamics are systematically studied. The paper is concluded in Sect. 5 with discussions.

2. Mathematical model

In this section, we present the binary fluid PFS model with MCL. In particular, the GNBC for the dynamics of moving contact lines is imposed at solid wall. The energy dissipation law for this system is obtained.

2.1. Governing equations

We introduce two conserved order parameters ϕ and ψ to represent local volume fraction of one phase and surfactant concentration respectively. ϕ is usually called phase-field variable which labels the two different phases with label -1 and 1. ψ is a fraction ranging from 0 to 1.

We first give the total free energy functional except for kinetic energy as follows [49]:

$$E_f(\phi,\psi) = E_{GL}(\phi) + E_{sur}(\psi) + E_{ad}(\phi,\psi) + E_{wf}(\phi). \tag{1}$$

In this expression, E_{GL} is given by the Ginzburg-Landau free energy with double-well potential in the bulk,

$$E_{GL}(\phi) = \int_\Omega \frac{\text{Cn}^2}{2}|\nabla\phi|^2 + \frac{1}{4}(\phi^2-1)^2 \mathrm{d}x, \tag{2}$$

where Cn is the Cahn number, which is determined by interface thickness and characteristic length. The quartic function $F(\phi) = (\phi^2-1)^2/4$ is "double well" potential which expresses a preference at pure phases $\phi = \pm 1$.

E_{sur} is the energy representing mixing entropy in binary surfactant-fluid system:

$$E_{sur}(\psi) = \int_\Omega \text{Pi}\big[\psi\ln\psi + (1-\psi)\ln(1-\psi)\big]\mathrm{d}x, \tag{3}$$

where Pi is the temperature-dependent constant. Here, a Flory-Huggins free energy is rather preferred as it possesses Langmuir isotherm relation [21].

The interfacial energy accounting for the adsorption of surfactant is given by

$$E_{ad}(\phi, \psi) = \int_{\Omega} \frac{1}{2\mathrm{Ex}} \psi \phi^2 - \frac{1}{4} \psi (1 - \phi^2)^2 \mathrm{d}x, \tag{4}$$

where Ex determines the bulk solubility. Hereby, $\psi \phi^2 / (2\mathrm{Ex})$ is an enthalpic term penalizing free surfactant in the respective phases, whereas the term $-\psi(1-\phi^2)^2/4$ represents local attraction of surfactant to an existing interface. Other approximations for E_{ad} are also available, for instance,

$$E_{ad}(\phi, \psi) = \int_{\Omega} \frac{1}{2\mathrm{Ex}} \psi \phi^2 - \frac{1}{2} \psi |\nabla \phi|^2 \mathrm{d}x, \qquad \text{or} \qquad E_{ad}(\phi, \psi) = \int_{\Omega} \frac{1}{2\mathrm{Ex}} \psi \phi^2 - \frac{1}{4} \psi (1 - \phi^2) \mathrm{d}x.$$

According to [22], (4) performs best in numerical experiments in comparison with the other two formulae. Hence, we will use (4) in our study. It is worth noting that the interplay of Pi and Ex yields the Langmuir adsorption isotherm [22,49].

Finally, we choose the wall energy E_{wf} as

$$E_{wf}(\phi) = \mathrm{Cn} \int_{\Gamma} \gamma_{wf}(\phi) \mathrm{d}S, \qquad \gamma_{wf}(\phi) = -\frac{\sqrt{2}}{3} \cos \theta_s \sin\left(\frac{\pi \phi}{2}\right) + \frac{\gamma_1 + \gamma_2}{2}, \tag{5}$$

where γ_1 and γ_2 are two fluid-solid surface tensions, θ_s is Young's angle determined through Young-Dupré equation $2\sqrt{2}/3 \cos \theta_s = \gamma_2 - \gamma_1$, and $\sin(\frac{\pi\phi}{2})$ is an interpolation function between ± 1. In consideration of asymptotic properties, another interpolation function $\frac{1}{2}\phi(3 - \phi^2)$ can also be used [62]. In this work, we prefer to use $\sin(\frac{\pi\phi}{2})$ as its all derivatives are smooth and bounded.

After taking the variational derivatives of the free energy E_f with respect to ψ and ϕ, one obtains the chemical potentials

$$\mu_\psi = \frac{\delta E_f}{\delta \psi} = \mathrm{Pi} \ln\left(\frac{\psi}{1 - \psi}\right) + \frac{1}{2\mathrm{Ex}} \phi^2 - \frac{1}{4}(\phi^2 - 1)^2, \tag{6}$$

$$\mu_\phi = \frac{\delta E_f}{\delta \phi} = -\mathrm{Cn}^2 \Delta \phi + \phi^3 - \phi + \frac{1}{\mathrm{Ex}} \psi \phi - \psi(\phi^3 - \phi). \tag{7}$$

Then the Cahn–Hilliard type governing equations are given by

$$\psi_t + \nabla \cdot (\mathbf{u}\psi) = \frac{1}{\mathrm{Pe}_\psi} \nabla \cdot M_\psi \nabla \mu_\psi, \tag{8}$$

$$\phi_t + \nabla \cdot (\mathbf{u}\phi) = \frac{1}{\mathrm{Pe}_\phi} \Delta \mu_\phi, \tag{9}$$

where Pe_ψ and Pe_ϕ are the Péclet numbers, and $\mathbf{u}$ is the velocity field. We choose the degenerate mobility $M_\psi = \psi(1 - \psi)$ which leads to the Fickian diffusion [21].

In addition, to take variable density and viscosity into account, we interpolate between two fluid densities and viscosities, i.e.,

$$\rho(\phi) = \frac{1 - \phi}{2} + \lambda_\rho \frac{1 + \phi}{2}, \qquad \eta(\phi) = \frac{1 - \phi}{2} + \lambda_\eta \frac{1 + \phi}{2},$$

where λ_ρ and λ_η are respectively the density ratio and viscosity ratio. Then using (9), we can modify the continuity equation as

$$\rho_t + \nabla \cdot (\mathbf{u}\rho) + \nabla \cdot \mathbf{J}_\rho = 0, \tag{10}$$

where the diffusive flux $\mathbf{J}_\rho = \frac{1 - \lambda_\rho}{2\mathrm{Pe}_\phi} \nabla \mu_\phi$ is included.

Following [63], we can derive the momentum equation for hydrodynamics as

$$\rho(\mathbf{u}_t + \mathbf{u} \cdot \nabla \mathbf{u}) + \mathbf{J}_\rho \cdot \nabla \mathbf{u} + \nabla p = \frac{1}{\mathrm{Re}} \nabla \cdot \left(\eta D(\mathbf{u})\right) - \frac{1}{\mathrm{WeCn}} (\phi \nabla \mu_\phi + \psi \nabla \mu_\psi), \tag{11}$$

where p is the pressure, and $D(\mathbf{u}) = \nabla \mathbf{u} + (\nabla \mathbf{u})^\top$ represents twice the strain rate. Here, Reynolds number Re and Weber number We are the dimensionless parameters, and $\phi \nabla \mu_\phi + \psi \nabla \mu_\psi$ is the capillary force. Note that, we neglect the gravitational force simply because we are focusing on the capillary effect. Moreover, (11) is supplemented with the incompressible condition

$$\nabla \cdot \mathbf{u} = 0. \tag{12}$$

2.2. Boundary conditions

On the solid wall Γ, the relaxation boundary condition associated with the ϕ-equation (9) reads

$$\phi_t + \mathbf{u}_\tau \cdot \nabla_\tau \phi = -\frac{1}{\mathrm{Pe}_s} L(\phi), \tag{13}$$

where Pe_s is the Péclet number, $\nabla_\tau = (\mathbf{I} - \mathbf{n} \otimes \mathbf{n})\nabla$ is the surface gradient, and $\mathbf{u}_\tau = (\mathbf{I} - \mathbf{n} \otimes \mathbf{n})\mathbf{u}$ is the tangential velocity on Γ, with $\mathbf{n}$ being the outward normal vector to Γ. In addition, $L(\phi)$ is the chemical potential on Γ defined by

$$L(\phi) = \mathrm{Cn}\partial_n\phi + \gamma'_{wf}(\phi). \tag{14}$$

In consideration of contact line dynamics, GNBC is imposed on Γ:

$$\frac{\mathbf{u}_s}{\mathrm{L}_s l_s} = \frac{L(\phi)\nabla_\tau\phi}{\mathrm{Ca}\eta} - \partial_n\mathbf{u}_\tau, \tag{15}$$

where $l_s(\phi) = (1 - \phi)/2 + \lambda_{l_s}(1 + \phi)/2$ is the dimensionless interpolating slip length, L_s and λ_{l_s} are the slip length of fluid 1 and the slip length ratio respectively, $\mathrm{Ca} = \mathrm{We}/\mathrm{Re}$ is the Capillary number. Given the wall velocity $\mathbf{u}_w$, $\mathbf{u}_s = \mathbf{u}_\tau - \mathbf{u}_w$ is the slip velocity on Γ. The GNBC establishes a linear response relation between the slip velocity $\mathbf{u}_s$ and the sum of the viscous stress $\partial_n\mathbf{u}_\tau$ and the uncompensated Young stress $L(\phi)\nabla_\tau\phi$. Moreover, we also need the following impermeability conditions

$$\partial_n\mu_\phi = 0, \qquad \partial_n\mu_\psi = 0, \qquad \mathbf{n} \cdot \mathbf{u} = 0 \qquad \text{on } \Gamma. \tag{16}$$

On the rest of boundaries, we impose the following natural boundary conditions, i.e.,

$$\partial_n\phi = 0, \qquad \partial_n\mu_\phi = 0, \qquad \partial_n\mu_\psi = 0, \qquad \partial_n\mathbf{u}_\tau = \mathbf{0}, \qquad \mathbf{n} \cdot \mathbf{u} = 0 \qquad \text{on } \partial\Omega/\Gamma. \tag{17}$$

2.3. Energy law of the model

The system of equations and the associated boundary conditions presented in Sections 2.1 and 2.2 constitutes a dissipative system, whose energy dissipation law will be shown in this subsection. To this end, we first define the total energy E_{tot} of the system as the sum of the kinetic energy E_k and the free energy E_f:

$$E_{tot}(\mathbf{u}, \phi, \psi) = E_k(\mathbf{u}, \rho) + E_f(\phi, \psi), \tag{18}$$

where $E_k(\mathbf{u}, \rho) = \mathrm{WeCn}\int_\Omega \rho|\mathbf{u}|^2 \mathrm{d}x/2$ and $E_f(\phi, \psi)$ is given in (1). Five types of dissipations contribute to the dissipative mechanism: the viscous dissipation (R_v), the slip dissipation (R_s), the diffusion dissipation in phase-field dynamics (R_d), the diffusion dissipation in surfactant dynamics (R_e), and the dissipation due to phase-field relaxation at the solid surface (R_r), namely,

$$R_v = \frac{\mathrm{CaCn}}{2}\left\|\sqrt{\eta}D(\mathbf{u})\right\|^2 := \frac{\mathrm{CaCn}}{2}\int_\Omega \eta\left\|D(\mathbf{u})\right\|_F^2 \mathrm{d}x, \qquad R_s = \frac{\mathrm{CaCn}}{\mathrm{L}_s}\left\|\sqrt{\eta/l_s}\mathbf{u}_s\right\|_\Gamma^2,$$

$$R_d = \frac{1}{\mathrm{Pe}_\phi}\left\|\nabla\mu_\phi\right\|^2, \qquad R_e = \frac{1}{\mathrm{Pe}_\psi}\left\|\sqrt{M_\psi}\nabla\mu_\psi\right\|^2, \qquad R_r = \frac{\mathrm{Cn}}{\mathrm{Pe}_s}\left\|L(\phi)\right\|_\Gamma^2, \tag{19}$$

where $\|\cdot\|$ and $\|\cdot\|_\Gamma$ are the L^2 norm in Ω and on Γ respectively, and $\|\cdot\|_F$ is the Frobenius norm for the matrix. With these concepts in hand, we can prove the following energy law.

Theorem 1. *Assume* $\mathbf{u}_w = \mathbf{0}$*, then the system* (6)–(17) *is a dissipative system satisfying the following energy dissipation law*

$$\frac{\mathrm{d}}{\mathrm{d}t}E_{tot} = -(R_v + R_s + R_d + R_e + R_r) \le 0. \tag{20}$$

Proof. We first use the modified continuity equation $\rho_t + \nabla \cdot (\mathbf{u}\rho) + \nabla \cdot \mathbf{J}_\rho = 0$ and integration by parts to obtain

$$\frac{\mathrm{d}}{\mathrm{d}t}\int_\Omega \frac{1}{2}\rho|\mathbf{u}|^2\mathrm{d}x = \int_\Omega \rho\mathbf{u} \cdot \mathbf{u}_t + \frac{1}{2}\rho_t|\mathbf{u}|^2\mathrm{d}x = \int_\Omega \mathbf{u} \cdot (\rho\mathbf{u}_t + \rho\mathbf{u} \cdot \nabla\mathbf{u} + \mathbf{J}_\rho \cdot \nabla\mathbf{u})\mathrm{d}x, \tag{21}$$

where non-penetration boundary conditions in (16) and (17) have been used in deriving the second equality. Then by taking the inner product of (11) with $\mathrm{WeCn}\mathbf{u}$ in Ω and using (21), we have

$$\frac{\mathrm{d}}{\mathrm{d}t}E_k + R_v - \mathrm{CaCn}\int_\Gamma \eta\mathbf{u}_\tau \cdot \partial_n\mathbf{u}_\tau \mathrm{d}S = -\int_\Omega \phi\mathbf{u} \cdot \nabla\mu_\phi + \psi\mathbf{u} \cdot \nabla\mu_\psi \mathrm{d}x. \tag{22}$$

Here, we have used the following integration by parts,

$$-\int_\Omega \mathbf{u} \cdot \left[\nabla \cdot (\eta D(\mathbf{u}))\right]\mathrm{d}x = \frac{1}{2}\left\|\sqrt{\eta}D(\mathbf{u})\right\|^2 - \int_\Gamma \eta\mathbf{u}_\tau \cdot \mathcal{P}[D(\mathbf{u})\mathbf{n}]\mathrm{d}S = \frac{1}{2}\left\|\sqrt{\eta}D(\mathbf{u})\right\|^2 - \int_\Gamma \eta\mathbf{u}_\tau \cdot \partial_n\mathbf{u}_\tau \mathrm{d}S,$$

where $\mathcal{P} := \mathbf{I} - \mathbf{n} \otimes \mathbf{n}$ represents the projection operator on Γ. By taking the inner product of (15) with $\mathrm{CaCn}\eta\mathbf{u}_\tau$ on Γ and using $\mathbf{u}_w = \mathbf{0}$, we arrive at

$$R_s = -\mathrm{CaCn}\int_\Gamma \eta\mathbf{u}_\tau \cdot \partial_n\mathbf{u}_\tau \mathrm{d}S + \mathrm{Cn}\int_\Gamma L(\phi)\mathbf{u}_\tau \cdot \nabla_\tau\phi \mathrm{d}S. \tag{23}$$

Taking the inner products of (8) and (6) with μ_ψ and ψ_t respectively in Ω, and collecting the results together with the homogeneous Neumann boundary conditions in (16) and (17), we have

$$-\frac{1}{\text{Pe}_\psi}\left\|\sqrt{M_\psi}\nabla\mu_\psi\right\|^2 = -\int_\Omega \psi\mathbf{u}\cdot\nabla\mu_\psi\,\mathrm{d}x + \int_\Omega \left(\text{Pi}\ln\left(\frac{\psi}{1-\psi}\right)+\frac{1}{2\text{Ex}}\phi^2-\frac{1}{4}(\phi^2-1)^2\right)\psi_t\,\mathrm{d}x. \tag{24}$$

Similar manipulations for (9) and (7) lead to

$$-\frac{1}{\text{Pe}_\phi}\left\|\nabla\mu_\phi\right\|^2 = -\int_\Omega \phi\mathbf{u}\cdot\nabla\mu_\phi\,\mathrm{d}x + \int_\Omega \left(-\text{Cn}^2\Delta\phi+\phi^3-\phi+\frac{1}{\text{Ex}}\psi\phi-\psi(\phi^3-\phi)\right)\phi_t\,\mathrm{d}x. \tag{25}$$

Moreover, taking the inner products of (13) and (14) with $\text{Cn}L(\phi)$ and $\text{Cn}\phi_t$ respectively on Γ, we have

$$-R_r = \text{Cn}\int_\Gamma L(\phi)\mathbf{u}_\tau\cdot\nabla_\tau\phi\,\mathrm{d}S + \text{Cn}\int_\Gamma \left(\text{Cn}\partial_n\phi+\gamma'_{wf}(\phi)\right)\phi_t\,\mathrm{d}S. \tag{26}$$

To conclude, we combine (22)–(26) and obtain

$$\begin{aligned}\frac{\mathrm{d}}{\mathrm{d}t}E_{tot} &= \frac{\mathrm{d}}{\mathrm{d}t}E_k + \frac{\mathrm{d}}{\mathrm{d}t}E_f \\ &= -(R_v+R_s+R_d+R_e+R_r)\leq 0. \quad \square\end{aligned}$$

Remark 1. It is worth noting that we only consider the fixed solid wall in our work, i.e., $\mathbf{u}_w=\mathbf{0}$, in the assumption of Theorem 1. Under this condition, the governing system satisfies an energy dissipation law. This assumption will continue to be considered in the discrete energy law in Theorem 2. In the case where $\mathbf{u}_w\neq\mathbf{0}$, external work power $-\text{L}_s^{-1}\int_\Gamma l_s^{-1}\eta\mathbf{u}_s\cdot\mathbf{u}_w\,\mathrm{d}S$ done by the wall to the flow will be included in the energy law (20).

3. Numerical method

In this section, we construct a set of energy stable schemes. We start with a first-order time-discrete scheme, whose energy stability can be rigorously proved. Then we extend it to a second-order version.

Since we are only interested in $\phi\in[-1,1]$, we can modify $F(\phi)=(\phi^2-1)^2/4$ to have a quadratic growth rate for $|\phi|>1$ [64]:

$$\widehat{F}(\phi)=\begin{cases}(\phi+1)^2 & \text{if } \phi<-1,\\(\phi^2-1)^2/4 & \text{if } -1\leq\phi\leq 1,\\(\phi-1)^2 & \text{if } \phi>1.\end{cases}$$

It is proved that this truncated $\widehat{F}(\phi)$ with quadratic growth at infinity can guarantee the boundedness of ϕ in the Ginzburg-Landau energy E_{GL}. Correspondingly, we use $\widehat{f}(\phi)=\widehat{F}'(\phi)$ to replace $\phi^3-\phi$ in (7). Hereafter, the notation $\widehat{\,\,}$ is omitted for convenience.

By using the convex splitting technique for the terms in (6) and using the stabilization method [65] for (7) and (9) with relaxation boundary condition (13)–(14), we can construct a first-order energy stable scheme. In addition, a splitting method based on pressure stabilization [57] is implemented to decouple the computation of velocity from pressure for the variable density Navier–Stokes equations with the GNBC.

3.1. First-order scheme

We give a first-order temporal discretized scheme for the system (6)–(17):

Step 1: Given the initial data ψ^0, ϕ^0, $p^{-1}=p^0=0$ and $\mathbf{u}^0$, we compute ψ^{n+1}, μ_ψ^{n+1}, ϕ^{n+1}, μ_ϕ^{n+1}, $\mathbf{u}^{n+1}$ for $n\geq 0$ by

$$\frac{\psi^{n+1}-\psi^n}{\Delta t}+\nabla\cdot(\mathbf{u}^{n+1}\psi^n)=\frac{1}{\text{Pe}_\psi}\nabla\cdot M_\psi^{n+1}\nabla\mu_\psi^{n+1}, \tag{27}$$

$$\mu_\psi^{n+1}=\text{Pi}\ln\left(\frac{\psi^{n+1}}{1-\psi^{n+1}}\right)+\frac{1}{2\text{Ex}}(\phi^n)^2-\frac{1}{4}\left((\phi^n)^2-1\right)^2, \tag{28}$$

$$\frac{\phi^{n+1}-\phi^n}{\Delta t}+\nabla\cdot(\mathbf{u}^{n+1}\phi^n)=\frac{1}{\text{Pe}_\phi}\Delta\mu_\phi^{n+1}, \tag{29}$$

$$\mu_\phi^{n+1}=-\text{Cn}^2\Delta\phi^{n+1}+s_1(\phi^{n+1}-\phi^n)+f(\phi^n)+\frac{1}{\text{Ex}}\psi^{n+1}\phi^{n+1}-\psi^{n+1}\left((\phi^n)^3-\phi^{n+1}\right), \tag{30}$$

$$\rho^n \frac{\mathbf{u}^{n+1} - \mathbf{u}^n}{\Delta t} + \rho^{n+1} \mathbf{u}^n \cdot \nabla \mathbf{u}^{n+1} + \mathbf{J}_\rho^{n+1} \cdot \nabla \mathbf{u}^{n+1} + \nabla(2p^n - p^{n-1})$$

$$= \frac{1}{\mathrm{Re}} \nabla \cdot \left(\eta^{n+1} D(\mathbf{u}^{n+1}) \right) - \frac{1}{\mathrm{WeCn}} (\phi^n \nabla \mu_\phi^{n+1} + \psi^n \nabla \mu_\psi^{n+1}) \tag{31}$$

$$- \frac{1}{2} \frac{\rho^{n+1} - \rho^n}{\Delta t} \mathbf{u}^{n+1} - \frac{1}{2} \nabla \cdot (\rho^{n+1} \mathbf{u}^n) \mathbf{u}^{n+1} - \frac{1}{2} (\nabla \cdot \mathbf{J}_\rho^{n+1}) \mathbf{u}^{n+1},$$

with boundary conditions

$$\frac{\phi^{n+1} - \phi^n}{\Delta t} + \mathbf{u}_\tau^{n+1} \cdot \nabla_\tau \phi^n = -\frac{1}{\mathrm{Pe}_s} L_\phi^{n+1} \qquad\qquad \text{on } \Gamma, \tag{32}$$

$$\frac{\mathbf{u}_s^{n+1}}{\mathrm{L}_s l_s^{n+1}} = \frac{L_\phi^{n+1} \nabla_\tau \phi^n}{\mathrm{Ca} \eta^{n+1}} - \partial_n \mathbf{u}_\tau^{n+1} \qquad\qquad \text{on } \Gamma, \tag{33}$$

$$\partial_n \mu_\phi^{n+1} = 0, \qquad \partial_n \mu_\psi^{n+1} = 0, \qquad \mathbf{n} \cdot \mathbf{u}^{n+1} = 0 \qquad\qquad \text{on } \Gamma, \tag{34}$$

$$\partial_n \phi^{n+1} = 0, \qquad \partial_n \mu_\phi^{n+1} = 0, \qquad \partial_n \mu_\psi^{n+1} = 0, \qquad \partial_n \mathbf{u}_\tau^{n+1} = \mathbf{0}, \qquad \mathbf{n} \cdot \mathbf{u}^{n+1} = 0 \qquad \text{on } \partial\Omega/\Gamma, \tag{35}$$

where

$$L_\phi^{n+1} = \mathrm{Cn} \partial_n \phi^{n+1} + s_2(\phi^{n+1} - \phi^n) + \gamma_{wf}'(\phi^n), \tag{36}$$

$$\rho^{n+1} = (1 - \phi^{n+1})/2 + \lambda_\rho (1 + \phi^{n+1})/2, \qquad \eta^{n+1} = (1 - \phi^{n+1})/2 + \lambda_\eta (1 + \phi^{n+1})/2, \tag{37}$$

$$l_s^{n+1} = (1 - \phi^{n+1})/2 + \lambda_{l_s} (1 + \phi^{n+1})/2, \qquad M_\psi^{n+1} = \psi^{n+1}(1 - \psi^{n+1}), \tag{38}$$

$$f(\phi^n) = \begin{cases} 2(\phi^n + 1) & \text{if } \phi^n < -1, \\ (\phi^n)^3 - \phi^n & \text{if } -1 \le \phi^n \le 1, \\ 2(\phi^n - 1) & \text{if } \phi^n > 1, \end{cases} \qquad \mathbf{J}_\rho^{n+1} = \frac{1 - \lambda_\rho}{2\mathrm{Pe}_\phi} \nabla \mu_\phi^{n+1}, \qquad \mathbf{u}_s^{n+1} = \mathbf{u}_\tau^{n+1} - \mathbf{u}_w. \tag{39}$$

Step 2: Update p^{n+1} for $n \ge 0$ by solving

$$\Delta(p^{n+1} - p^n) = \frac{\bar{\rho}}{\Delta t} \nabla \cdot \mathbf{u}^{n+1}, \tag{40}$$

with $\bar{\rho} = \min(1, \lambda_\rho)$ and boundary condition

$$\mathbf{n} \cdot \nabla p^{n+1} = 0 \qquad \text{on } \partial\Omega.$$

It should be noted that when discretizing the momentum equation (11), we include three more terms in (31), which serves as a first-order approximation of $(\rho_t + \nabla \cdot (\mathbf{u}\rho) + \nabla \cdot \mathbf{J}_\rho)\mathbf{u}/2$ at t^{n+1}. These additional terms are approximately zero due to the modified continuity equation (10). Hence, (31) is indeed a consistent first-order approximation to (11) in time.

For the proposed scheme (27)–(40), we have the following discrete energy law.

Theorem 2. *Assume that $\mathbf{u}_w = \mathbf{0}$, $s_1 \ge 1$, $s_2 \ge |\frac{\sqrt{2}\pi^2}{24} \cos\theta_s|$, and the scheme (27)–(40) is well-defined with a logarithmic potential, then the scheme (27)–(40) is unconditionally energy stable, and satisfies the following discrete dissipation law:*

$$E_{tot}^{n+1} - E_{tot}^n \le -\frac{\Delta t \mathrm{CaCn}}{2} \left\| \sqrt{\eta^{n+1}} D(\mathbf{u}^{n+1}) \right\|^2 - \frac{\Delta t}{\mathrm{Pe}_\psi} \left\| \sqrt{M_\psi^{n+1}} \nabla \mu_\psi^{n+1} \right\|^2 - \frac{\Delta t}{\mathrm{Pe}_\phi} \left\| \nabla \mu_\phi^{n+1} \right\|^2$$

$$- \frac{\Delta t \mathrm{CaCn}}{\mathrm{L}_s} \left\| \sqrt{\eta^{n+1}/l_s^{n+1}} \mathbf{u}_s^{n+1} \right\|_\Gamma^2 - \frac{\Delta t \mathrm{Cn}}{\mathrm{Pe}_s} \left\| L_\phi^{n+1} \right\|_\Gamma^2 \le 0, \tag{41}$$

where

$$E_{tot}^n = E_k(\mathbf{u}^n, \rho^n) + E_{GL}(\phi^n) + E_{sur}(\psi^n) + E_{ad}(\phi^n, \psi^n) + E_{wf}(\phi^n) + \frac{\Delta t^2 \mathrm{WeCn}}{2\bar{\rho}} \left\| \nabla p^n \right\|^2.$$

Here, E_{GL}, E_{sur}, E_{ad}, E_{wf} and E_k are defined in (2)–(5) and (18) respectively.

Proof. We first take the inner products of (27) and (28) with $\Delta t \mu_\psi^{n+1}$ and $\psi^{n+1} - \psi^n$ in Ω respectively. Summing the results up and using the integration by parts and the homogeneous Neumann boundary condition, we obtain

$$\int_\Omega (\psi^{n+1} - \psi^n) \left(\mathrm{Pi} \ln\left(\frac{\psi^{n+1}}{1 - \psi^{n+1}} \right) + \frac{1}{2\mathrm{Ex}} (\phi^n)^2 - \frac{1}{4} \left((\phi^n)^2 - 1 \right)^2 \right) \mathrm{d}x - \Delta t \int_\Omega \psi^n \mathbf{u}^{n+1} \cdot \nabla \mu_\psi^{n+1} \mathrm{d}x$$

$$= -\frac{\Delta t}{\mathrm{Pe}_\psi} \left\| \sqrt{M_\psi^{n+1}} \nabla \mu_\psi^{n+1} \right\|^2. \tag{42}$$

Using the inequality

$$(a - b)\ln a \geq (a \ln a - a) - (b \ln b - b),$$

we can estimate the left side of (42) and recast it into an inequality

$$E_{sur}(\psi^{n+1}) - E_{sur}(\psi^n) + E_{ad}(\phi^n, \psi^{n+1}) - E_{ad}(\phi^n, \psi^n) - \Delta t \int_\Omega \psi^n \mathbf{u}^{n+1} \cdot \nabla \mu_\psi^{n+1} dx$$

$$\leq -\frac{\Delta t}{\mathrm{Pe}_\psi} \left\| \sqrt{M_\psi^{n+1}} \nabla \mu_\psi^{n+1} \right\|^2. \tag{43}$$

By taking the inner products of (29) and (30) with $\Delta t \mu_\phi^{n+1}$ and $\phi^{n+1} - \phi^n$ respectively in Ω and combining them, we have

$$\int_\Omega (\phi^{n+1} - \phi^n)\left(-\mathrm{Cn}^2 \Delta \phi^{n+1} + s_1(\phi^{n+1} - \phi^n) + f(\phi^n) - \psi^{n+1}((\phi^n)^3 - \phi^{n+1}) + \frac{1}{\mathrm{Ex}} \psi^{n+1} \phi^{n+1} \right) dx$$

$$= \Delta t \int_\Omega \phi^n \mathbf{u}^{n+1} \cdot \nabla \mu_\phi^{n+1} dx - \frac{\Delta t}{\mathrm{Pe}_\phi} \left\| \nabla \mu_\phi^{n+1} \right\|^2. \tag{44}$$

Due to the existence of logarithmic potential in (28) of the scheme, it follows that $0 < \psi^{n+1} < 1$. Using integration by parts and the inequality

$$a(a - b) = \frac{1}{2}|a|^2 - \frac{1}{2}|b|^2 + \frac{1}{2}|a - b|^2 \geq \frac{1}{2}(|a|^2 - |b|^2) \tag{45}$$

recursively, we can recast (44) into

$$\Delta t \int_\Omega \phi^n \mathbf{u}^{n+1} \cdot \nabla \mu_\phi^{n+1} dx - \frac{\Delta t}{\mathrm{Pe}_\phi} \left\| \nabla \mu_\phi^{n+1} \right\|^2$$

$$\geq \int_\Omega \mathrm{Cn}^2 (\nabla \phi^{n+1} - \nabla \phi^n) \nabla \phi^{n+1} dx - \mathrm{Cn}^2 \int_\Gamma (\phi^{n+1} - \phi^n) \partial_n \phi^{n+1} dS$$

$$+ \int_\Omega \left\{ \left(s_1 - \frac{1}{2}f'(\sigma^n)\right)|\phi^{n+1} - \phi^n|^2 + F(\phi^{n+1}) - F(\phi^n) + \frac{1}{2\mathrm{Ex}} \psi^{n+1} \left(|\phi^{n+1}|^2 - |\phi^n|^2\right) \right.$$

$$\left. + \frac{1}{2} \psi^{n+1} \left[\left(|\phi^n|^2 - |\phi^{n+1}|^2\right)|\phi^n|^2 + \left(|\phi^{n+1}|^2 - |\phi^n|^2\right) \right] \right\} dx \tag{46}$$

$$\geq E_{GL}(\phi^{n+1}) - E_{GL}(\phi^n) + E_{ad}(\phi^{n+1}, \psi^{n+1}) - E_{ad}(\phi^n, \psi^{n+1})$$

$$- \mathrm{Cn}^2 \int_\Gamma (\phi^{n+1} - \phi^n) \partial_n \phi^{n+1} dS,$$

where the first inequality is obtained by the Taylor expansion of $F(\phi)$ at ϕ^n,

$$f(\phi^n)(\phi^{n+1} - \phi^n) = F(\phi^{n+1}) - F(\phi^n) - \frac{1}{2}f'(\sigma^n)|\phi^{n+1} - \phi^n|^2,$$

for some $\sigma^n \in \left[\min\{\phi^{n+1}, \phi^n\}, \max\{\phi^{n+1}, \phi^n\}\right]$, and the last inequality is due to the condition that $s_1 \geq 1$. Then, by taking the inner products of the equation (32) and (36) with $\Delta t \mathrm{Cn} L_\phi^{n+1}$ and $\mathrm{Cn}(\phi^{n+1} - \phi^n)$ respectively on Γ, we have

$$\mathrm{Cn} \int_\Gamma (\phi^{n+1} - \phi^n)\left(\mathrm{Cn}\partial_n \phi^{n+1} + s_2(\phi^{n+1} - \phi^n) + \gamma'_{wf}(\phi^n)\right) dS$$

$$= -\Delta t \mathrm{Cn} \int_\Gamma L_\phi^{n+1} \mathbf{u}^{n+1} \cdot \nabla_\tau \phi^n dS - \frac{\Delta t \mathrm{Cn}}{\mathrm{Pe}_s} \left\| L_\phi^{n+1} \right\|_\Gamma^2. \tag{47}$$

A Taylor expansion of γ_{wf} at ϕ^n leads to

$$\gamma'_{wf}(\phi^n)(\phi^{n+1} - \phi^n) = \gamma_{wf}(\phi^{n+1}) - \gamma_{wf}(\phi^n) - \frac{1}{2}\gamma''_{wf}(\zeta^n)|\phi^{n+1} - \phi^n|^2,$$

for some $\zeta^n \in \left[\min\{\phi^{n+1}, \phi^n\}, \max\{\phi^{n+1}, \phi^n\}\right]$. Then (47) can be recast as

$$-\Delta t \mathrm{Cn} \int_\Gamma L_\phi^{n+1} \mathbf{u}^{n+1} \cdot \nabla_\tau \phi^n - \frac{\Delta t \mathrm{Cn}}{\mathrm{Pe}_s} \left\| L_\phi^{n+1} \right\|_\Gamma^2$$

$$= \mathrm{Cn} \int_{\Gamma} \left(s_2 - \frac{1}{2}\gamma''_{wf}(\zeta^n) \right) |\phi^{n+1} - \phi^n|^2 + \gamma_{wf}(\phi^{n+1}) - \gamma_{wf}(\phi^n)\mathrm{d}S + \mathrm{Cn}^2 \int_{\Gamma} (\phi^{n+1} - \phi^n)\partial_n \phi^{n+1}\mathrm{d}S$$

$$\geq E_{wf}(\phi^{n+1}) - E_{wf}(\phi^n) + \mathrm{Cn}^2 \int_{\Gamma} (\phi^{n+1} - \phi^n)\partial_n \phi^{n+1}\mathrm{d}S, \tag{48}$$

where the last inequality is due to the condition that $s_2 \geq |\frac{\sqrt{2}\pi^2}{24}\cos\theta_s|$.

We now consider the Navier-Stokes equations with the GNBC. Using integration by parts and boundary conditions $\partial_n \mu_\phi^{n+1} = 0$ and $\mathbf{n} \cdot \mathbf{u}^n = 0$, we can derive

$$\int_{\Omega} \left((\rho^{n+1}\mathbf{u}^n \cdot \nabla)\mathbf{u}^{n+1} + \frac{1}{2}(\nabla \cdot (\rho^{n+1}\mathbf{u}^n))\mathbf{u}^{n+1} \right) \cdot \mathbf{u}^{n+1}\mathrm{d}x = \frac{1}{2}\int_{\partial\Omega} \mathbf{n} \cdot (\rho^{n+1}\mathbf{u}^n)|\mathbf{u}^{n+1}|^2\mathrm{d}x = 0, \tag{49}$$

$$\int_{\Omega} \left(\mathbf{J}_\rho^{n+1} \cdot \nabla\mathbf{u}^{n+1} + \frac{1}{2}(\nabla \cdot \mathbf{J}_\rho^{n+1})\mathbf{u}^{n+1} \right) \cdot \mathbf{u}^{n+1}\mathrm{d}x = \frac{1}{2}\int_{\partial\Omega} \mathbf{n} \cdot \mathbf{J}_\rho^{n+1}|\mathbf{u}^{n+1}|^2\mathrm{d}x = 0. \tag{50}$$

Taking the inner product of (31) with $\Delta t\,\mathrm{WeCn}\mathbf{u}^{n+1}$ and using the equalities (49) and (50) and integration by parts, we obtain

$$\mathrm{WeCn} \int_{\Omega} \rho^n(\mathbf{u}^{n+1} - \mathbf{u}^n) \cdot \mathbf{u}^{n+1}\mathrm{d}x - \Delta t\,\mathrm{WeCn} \int_{\Omega} (2p^n - p^{n-1})\nabla \cdot \mathbf{u}^{n+1}\mathrm{d}x$$

$$= -\frac{\Delta t\,\mathrm{CaCn}}{2} \left\| \sqrt{\eta^{n+1}} D(\mathbf{u}^{n+1}) \right\|^2 + \Delta t\,\mathrm{CaCn} \int_{\Gamma} \eta^{n+1}\mathbf{u}_\tau^{n+1} \cdot \partial_n \mathbf{u}_\tau^{n+1}\mathrm{d}S$$

$$\quad - \Delta t \int_{\Omega} (\phi^n \nabla\mu_\phi^{n+1} + \psi^n \nabla\mu_\psi^{n+1}) \cdot \mathbf{u}^{n+1}\mathrm{d}x - \frac{\mathrm{WeCn}}{2} \int_{\Omega} (\rho^{n+1} - \rho^n)|\mathbf{u}^{n+1}|^2\mathrm{d}x, \tag{51}$$

where we have used the equality

$$\int_{\Omega} \nabla(2p^n - p^{n-1}) \cdot \mathbf{u}^{n+1}\mathrm{d}x = -\int_{\Omega} (2p^n - p^{n-1})\nabla \cdot \mathbf{u}^{n+1}\mathrm{d}x,$$

due to $\mathbf{n} \cdot \mathbf{u}^{n+1} = 0$ on $\partial\Omega$.

We now consider each term in (51) separately. Direct calculations lead to

$$\mathrm{WeCn} \int_{\Omega} \rho^n(\mathbf{u}^{n+1} - \mathbf{u}^n) \cdot \mathbf{u}^{n+1}\mathrm{d}x + \frac{\mathrm{WeCn}}{2} \int_{\Omega} (\rho^{n+1} - \rho^n)|\mathbf{u}^{n+1}|^2\mathrm{d}x$$

$$= \frac{\mathrm{WeCn}}{2} \int_{\Omega} \rho^{n+1}|\mathbf{u}^{n+1}|^2\mathrm{d}x - \frac{\mathrm{WeCn}}{2} \int_{\Omega} \rho^n|\mathbf{u}^n|^2\mathrm{d}x + \frac{\mathrm{WeCn}}{2} \int_{\Omega} \rho^n|\mathbf{u}^{n+1} - \mathbf{u}^n|^2\mathrm{d}x \tag{52}$$

$$= E_k(\mathbf{u}^{n+1}, \rho^{n+1}) - E_k(\mathbf{u}^n, \rho^n) + \frac{\mathrm{WeCn}}{2} \int_{\Omega} \rho^n|\mathbf{u}^{n+1} - \mathbf{u}^n|^2\mathrm{d}x.$$

According to (40) and the Helmholtz-Hodge decomposition, $\nabla(p^{n+1} - p^n)$ is the unique projection of $\frac{\bar{\rho}}{\Delta t}\mathbf{u}^{n+1}$ on the linear subspace of gradient fields with homogeneous Neumann boundary condition. Thus, $\nabla(p^{n+1} - p^n) - \nabla(p^n - p^{n-1})$ is the unique projection of $\frac{\bar{\rho}}{\Delta t}(\mathbf{u}^{n+1} - \mathbf{u}^n)$. Moreover,

$$\left\| \nabla(p^{n+1} - p^n) - \nabla(p^n - p^{n-1}) \right\| \leq \frac{\bar{\rho}}{\Delta t} \left\| \mathbf{u}^{n+1} - \mathbf{u}^n \right\|.$$

Then using (45), we have

$$\int_{\Omega} (2p^n - p^{n-1})\nabla \cdot \mathbf{u}^{n+1}\mathrm{d}x$$

$$= -\frac{\Delta t}{\bar{\rho}} \int_{\Omega} (p^{n+1} - 2p^n + p^{n-1})\Delta(p^{n+1} - p^n)\mathrm{d}x + \frac{\Delta t}{\bar{\rho}} \int_{\Omega} p^{n+1}\Delta(p^{n+1} - p^n)\mathrm{d}x$$

$$= \frac{\Delta t}{2\bar{\rho}} \left\| \nabla(p^{n+1} - 2p^n + p^{n-1}) \right\|^2 - \frac{\Delta t}{2\bar{\rho}} \left(\left\| \nabla p^{n+1} \right\|^2 - \left\| \nabla p^n \right\|^2 \right) - \frac{\Delta t}{2\bar{\rho}} \left\| \nabla(p^n - p^{n-1}) \right\|^2$$

$$\leq \frac{\bar{\rho}}{2\Delta t} \left\| \mathbf{u}^{n+1} - \mathbf{u}^n \right\|^2 - \frac{\Delta t}{2\bar{\rho}} \left(\left\| \nabla p^{n+1} \right\|^2 - \left\| \nabla p^n \right\|^2 \right)$$

$$\leq \frac{1}{2\Delta t} \int_{\Omega} \rho^n |\mathbf{u}^{n+1} - \mathbf{u}^n|^2 dx - \frac{\Delta t}{2\bar{\rho}} \left(\left\| \nabla p^{n+1} \right\|^2 - \left\| \nabla p^n \right\|^2 \right), \tag{53}$$

where the last inequality is due to the definition of $\bar{\rho}$. According to (33) and $\mathbf{u}_w = \mathbf{0}$, the boundary term in (51) is rewritten as

$$\int_{\Gamma} \eta^{n+1} \mathbf{u}_\tau^{n+1} \cdot \partial_n \mathbf{u}_\tau^{n+1} dS = \int_{\Gamma} \mathbf{u}_\tau^{n+1} \cdot \left(\frac{L_\phi^{n+1} \nabla_\tau \phi^n}{\mathrm{Ca}} - \frac{\eta^{n+1} \mathbf{u}_s^{n+1}}{\mathrm{L}_s l_s^{n+1}} \right) dS$$

$$= \frac{1}{\mathrm{Ca}} \int_{\Gamma} L_\phi^{n+1} \mathbf{u}_\tau^{n+1} \cdot \nabla_\tau \phi^n dS - \frac{1}{\mathrm{L}_s} \left\| \sqrt{\eta^{n+1}/l_s^{n+1}} \mathbf{u}_s^{n+1} \right\|_\Gamma^2. \tag{54}$$

Combining (52)–(54), we can recast (51) into

$$E_k(\mathbf{u}^{n+1}, \rho^{n+1}) - E_k(\mathbf{u}^n, \rho^n) + \frac{\Delta t^2 \mathrm{WeCn}}{2\bar{\rho}} \left(\left\| \nabla p^{n+1} \right\|^2 - \left\| \nabla p^n \right\|^2 \right)$$

$$\leq -\frac{\Delta t \mathrm{CaCn}}{2} \left\| \sqrt{\eta^{n+1}} D(\mathbf{u}^{n+1}) \right\|^2 - \frac{\Delta t \mathrm{CaCn}}{\mathrm{L}_s} \left\| \sqrt{\eta^{n+1}/l_s^{n+1}} \mathbf{u}_s^{n+1} \right\|_\Gamma^2$$

$$- \Delta t \int_{\Omega} (\phi^n \nabla \mu_\phi^{n+1} + \psi^n \nabla \mu_\psi^{n+1}) \cdot \mathbf{u}^{n+1} dx + \Delta t \mathrm{Cn} \int_{\Gamma} L_\phi^{n+1} \mathbf{u}_\tau^{n+1} \cdot \nabla_\tau \phi^n dS. \tag{55}$$

Finally, collecting (43), (46), (48) and (55), we arrive at the desired energy inequality. $\square$

Remark 2. At a first glance, the proposed scheme (27)–(28) presents a difficulty in solving a nonlinear system in ψ^{n+1} due to the implicit treatment of the mobility M_ψ^{n+1}. However, this nonlinearity is weak since the second order derivative term is linear in ψ^{n+1} and nonlinearity only enters lower terms, i.e., (27)–(28) is equivalent to

$$\frac{\psi^{n+1} - \psi^n}{\Delta t} + \nabla \cdot (\mathbf{u}^{n+1} \psi^n) = \frac{\mathrm{Pi}}{\mathrm{Pe}_\psi} \Delta \psi^{n+1} + \frac{1}{\mathrm{Pe}_\psi} \nabla \cdot M_\psi^{n+1} \nabla \left(\frac{1}{2\mathrm{Ex}} (\phi^n)^2 - \frac{1}{4} ((\phi^n)^2 - 1)^2 \right). \tag{56}$$

The numerical stiffness of this equation mainly comes from the second order term $\Delta \psi$ which is already treated implicitly. To further remove the nonlinearity, we can replace M_ψ^{n+1} in (56) by M_ψ^n, leading to a linear system in ψ^{n+1},

$$\frac{\psi^{n+1} - \psi^n}{\Delta t} + \nabla \cdot (\mathbf{u}^{n+1} \psi^n) = \frac{\mathrm{Pi}}{\mathrm{Pe}_\psi} \Delta \psi^{n+1} + \frac{1}{\mathrm{Pe}_\psi} \nabla \cdot M_\psi^n \nabla \left(\frac{1}{2\mathrm{Ex}} (\phi^n)^2 - \frac{1}{4} ((\phi^n)^2 - 1)^2 \right), \tag{57}$$

associated with the boundary conditions $\mathrm{Pi}\partial_n \psi^{n+1} + M_\psi^n \partial_n ((\phi^n)^2/(2\mathrm{Ex}) - ((\phi^n)^2 - 1)^2/4) = 0$ on Γ and $\partial_n \psi^{n+1} = 0$ on $\partial\Omega/\Gamma$. This recovers the scheme in [18] in the absence of velocity field $\mathbf{u}^{n+1}$. However, in comparison to (56), the scheme (57) does not yields the discrete energy stability rigorously, since the following inequality does not hold:

$$\int_{\Omega} \left(M_\psi^{n+1} \nabla \left(\mathrm{Pi} \ln \frac{\psi^{n+1}}{1 - \psi^{n+1}} \right) + M_\psi^n \nabla \left(\frac{1}{2\mathrm{Ex}} (\phi^n)^2 - \frac{1}{4} ((\phi^n)^2 - 1)^2 \right) \right) \cdot \nabla \mu_\psi^{n+1} dx \geq 0.$$

It should be also noted that if the mobility in (27)–(28) is treated explicitly as M_ψ^n, we recover the scheme in [51], which has been proved to be energy stable and bound-preserving in the absence of velocity field.

3.2. Second-order scheme

Following the discussion of updating ψ^{n+1} in Remark 2, we propose the linear and decoupled second-order scheme (58)–(72) using second-order BDF discretization:

Step 1: Given the data $\psi^0, \psi^1, \phi^0, \phi^1, p^1, \varphi^0 = \varphi^1 = 0, \mathbf{u}^0$ and $\mathbf{u}^1$, we first compute $\psi^{n+1}, \mu_\psi^{n+1}, \phi^{n+1}, \mu_\phi^{n+1}, \mathbf{u}^{n+1}$ for $n \geq 1$ by

$$\frac{3\psi^{n+1} - 4\psi^n + \psi^{n-1}}{2\Delta t} + \nabla \cdot (\mathbf{u}^* \psi^*) = \frac{\mathrm{Pi}}{\mathrm{Pe}_\psi} \Delta \psi^{n+1} + \frac{1}{\mathrm{Pe}_\psi} \nabla \cdot M_\psi^* \nabla \left(\frac{1}{2\mathrm{Ex}} (\phi^*)^2 - \frac{1}{4} ((\phi^*)^2 - 1)^2 \right), \tag{58}$$

$$\mu_\psi^{n+1} = \mathrm{Pi} \ln \left(\frac{\psi^{n+1}}{1 - \psi^{n+1}} \right) + \frac{1}{2\mathrm{Ex}} (\phi^*)^2 - \frac{1}{4} ((\phi^*)^2 - 1)^2, \tag{59}$$

$$\frac{3\phi^{n+1} - 4\phi^n + \phi^{n-1}}{2\Delta t} + \nabla \cdot (\mathbf{u}^* \psi^*) = \frac{1}{\mathrm{Pe}_\phi} \Delta \mu_\phi^{n+1}, \tag{60}$$

$$\mu_\phi^{n+1} = -\mathrm{Cn}^2 \Delta \phi^{n+1} + s_1(\phi^{n+1} - \phi^*) + f(\phi^*) + \frac{1}{\mathrm{Ex}} \psi^{n+1} \phi^{n+1} - \psi^{n+1} ((\phi^*)^3 - \phi^{n+1}), \tag{61}$$

$$\rho^{n+1}\frac{3\mathbf{u}^{n+1}-4\mathbf{u}^n+\mathbf{u}^{n-1}}{2\Delta t}+\rho^{n+1}\mathbf{u}^*\cdot\nabla\mathbf{u}^*+\mathbf{J}_\rho^{n+1}\cdot\nabla\mathbf{u}^*+\nabla(p^n+\frac{4}{3}\varphi^n-\frac{1}{3}\varphi^{n-1})$$
$$=\frac{1}{\mathrm{Re}}\left(\eta^{n+1}\Delta\mathbf{u}^{n+1}+\nabla\eta^{n+1}\cdot D(\mathbf{u}^*)\right)-\frac{1}{\mathrm{WeCn}}(\phi^{n+1}\nabla\mu_\phi^{n+1}+\psi^{n+1}\nabla\mu_\psi^{n+1}),$$

(62)

with boundary conditions

$$\frac{3\phi^{n+1}-4\phi^n+\phi^{n-1}}{2\Delta t}+\mathbf{u}_\tau^*\cdot\nabla_\tau\phi^*=-\frac{1}{\mathrm{Pe}_s}L_\phi^{n+1} \qquad\qquad \text{on } \Gamma,$$

(63)

$$\frac{\mathbf{u}_s^{n+1}}{\mathrm{L}_s l_s^{n+1}}=\frac{L_\phi^{n+1}\nabla_\tau\phi^{n+1}}{\mathrm{Ca}\eta^{n+1}}-\partial_n\mathbf{u}_\tau^{n+1} \qquad\qquad \text{on } \Gamma,$$

(64)

$$\partial_n\mu_\phi^{n+1}=0, \qquad \mathrm{Pi}\partial_n\psi^{n+1}+M_\psi^*\partial_n\left(\frac{1}{2\mathrm{Ex}}(\phi^*)^2-\frac{1}{4}\left((\phi^*)^2-1\right)^2\right)=0, \qquad \mathbf{n}\cdot\mathbf{u}^{n+1}=0 \qquad \text{on } \Gamma,$$

(65)

$$\partial_n\phi^{n+1}=0, \qquad \partial_n\mu_\phi^{n+1}=0, \qquad \partial_n\psi^{n+1}=0, \qquad \partial_n\mathbf{u}_\tau^{n+1}=\mathbf{0}, \qquad \mathbf{n}\cdot\mathbf{u}^{n+1}=0 \qquad \text{on } \partial\Omega/\Gamma,$$

(66)

where

$$\psi^*=2\psi^n-\psi^{n-1}, \qquad \phi^*=2\phi^n-\phi^{n-1}, \qquad \mathbf{u}^*=2\mathbf{u}^n-\mathbf{u}^{n-1},$$

(67)

$$L_\phi^{n+1}=\mathrm{Cn}\partial_n\phi^{n+1}+s_2(\phi^{n+1}-\phi^*)+\gamma_{wf}'(\phi^*),$$

(68)

$$\rho^{n+1}=(1-\phi^{n+1})/2+\lambda_\rho(1+\phi^{n+1})/2, \qquad \eta^{n+1}=(1-\phi^{n+1})/2+\lambda_\eta(1+\phi^{n+1})/2,$$

(69)

$$l_s^{n+1}=(1-\phi^{n+1})/2+\lambda_{l_s}(1+\phi^{n+1})/2, \qquad M_\psi^*=\psi^*(1-\psi^*),$$

(70)

$$f(\phi^*)=\begin{cases}2(\phi^*+1) & \text{if } \phi^*<-1,\\(\phi^*)^3-\phi^* & \text{if } -1\le\phi^*\le1, \\ 2(\phi^*-1) & \text{if } \phi^*>1,\end{cases} \qquad \mathbf{J}_\rho^{n+1}=\frac{1-\lambda_\rho}{2\mathrm{Pe}_\phi}\nabla\mu_\phi^{n+1}, \qquad \mathbf{u}_s^{n+1}=\mathbf{u}_\tau^{n+1}-\mathbf{u}_w.$$

(71)

Step 2: Update p^{n+1} for $n\ge1$ by solving

$$\Delta\varphi^{n+1}=\frac{3\bar\rho}{2\Delta t}\nabla\cdot\mathbf{u}^{n+1},$$
$$p^{n+1}=p^n+\varphi^{n+1}-\eta^{n+1}\nabla\cdot\mathbf{u}^{n+1},$$

(72)

with $\bar\rho=\min(1,\lambda_\rho)$ and boundary condition

$$\mathbf{n}\cdot\nabla\varphi^{n+1}=0 \qquad \text{on } \partial\Omega.$$

Here, the data ψ^1, ϕ^1, p^1 and $\mathbf{u}^1$ are obtained using the first-order scheme (27)–(40). The proposed scheme (58)–(72) is decoupled for ψ^{n+1}, ϕ^{n+1}, $\mathbf{u}^{n+1}$ and p^{n+1}, and constitutes linear systems for ψ^{n+1}, ϕ^{n+1}, $\mathbf{u}^{n+1}$ and p^{n+1}. Thus, they can be solved efficiently by using linear solvers.

Remark 3. The discrete energy law of the second-order schemes for the NS-PFS-MCL model is still open. The main difficulties arise from the singularity in Flory-Huggins potential, the nonlinear coupling $\psi\phi^2$ and $\psi(\phi^2-1)^2$ between phase-field variable and surfactant concentration, the nonlinear coupling between the variables ψ, ϕ and the velocity through convection terms and stress terms, and the coupling in the variable density and viscosity. The nonlinear coupling between the velocity and the phase-field variable on the MCL boundary poses another challenge for proving the energy stability. Recently, the supplementary variable method has been developed by introducing an appropriate number of supplementary variables to the thermodynamically consistent partial differential equation system, including its energy equation and other derived equations [66]. This method enables the construction of thermodynamically consistent numerical algorithms for such systems. More recently, new theoretical frameworks have been introduced to directly analyze the stability of the Cahn-Hilliard equation [67,68]. These techniques can be valuable for the construction of provable energy stable second-order schemes for the NS-PFS-MCL model. Even though the energy stability for the second-order scheme is not easy to be proved analytically, the numerical result in Sect. 4.2 has shown that it is quite stable with the property of energy decay.

3.3. Numerical implementation

We first regularize the logarithmic potential $G(\psi)=\psi\ln\psi+(1-\psi)\ln(1-\psi)$ in (3) from the domain $(0,1)$ to $(-\infty,+\infty)$ to avoid the singularity. For any $\xi>0$, the regularized logarithmic potential [69] can be written as

$$\widehat{G}(\psi)=\begin{cases}\psi\ln\psi+\frac{(1-\psi)^2}{2\xi}+(1-\psi)\ln\xi-\frac{\xi}{2} & \text{if } \psi\ge1-\xi,\\\psi\ln\psi+(1-\psi)\ln(1-\psi) & \text{if } \xi<\psi<1-\xi,\\(1-\psi)\ln(1-\psi)+\frac{\psi^2}{2\xi}+\psi\ln\xi-\frac{\xi}{2} & \text{if } \psi\le\xi,\end{cases}$$

and when $\xi \to 0$, $\widehat{G}(\psi) \to G(\psi)$. In the numerical experiments, we focus on the NS-PFS-MCL model formulated with the regularized function $\widehat{G}(\psi)$. This modification makes the computation of μ_ψ^{n+1} in (28) and (59) free from singularities. The ^ is omitted in the notation for convenience.

The finite difference method is adopted for space discretization in our numerical implements. The first-order scheme (27)–(40) form a nonlinear coupled system. Nevertheless, the coupling system can be solved by either using a simple sub-iteration process or decoupling the system with a lagged velocity for the convection terms. In our simulations, instead of using sub-iterations, we treat the nonlinear convection terms explicitly in (27)–(32), i.e., $\nabla \cdot (\mathbf{u}^{n+1}\psi^n)$ as $\nabla \cdot (\mathbf{u}^n\psi^n)$ in (27), $\nabla \cdot (\mathbf{u}^{n+1}\phi^n)$ as $\nabla \cdot (\mathbf{u}^n\phi^n)$ in (29), $\rho^{n+1}\mathbf{u}^n \cdot \nabla \mathbf{u}^{n+1} + \mathbf{J}_\rho^{n+1} \cdot \nabla \mathbf{u}^{n+1}$ as $\rho^{n+1}\mathbf{u}^n \cdot \nabla \mathbf{u}^n + \mathbf{J}_\rho^{n+1} \cdot \nabla \mathbf{u}^n$ in (31), $\mathbf{u}_\tau^{n+1} \cdot \nabla_\tau \phi^n$ as $\mathbf{u}_\tau^n \cdot \nabla_\tau \phi^n$ in (32), which can decouple Cahn-Hilliard type equations (27)–(30) from Navier-Stokes equation (31). Then ψ^{n+1}, ϕ^{n+1}, $\mathbf{u}^{n+1}$ and p^{n+1} can be solved in order. We also decouple velocity components in (31) by writing the viscous stress term as

$$\nabla \cdot \left(\eta D(\mathbf{u}) \right) = \eta \Delta \mathbf{u} + \nabla \eta \cdot D(\mathbf{u}),$$

where the first term is treated implicitly and the second term is treated explicitly. This could greatly remove stiffness of viscous term, even though the second term would introduce some mild CFL constraint. The resulting system has only variable coefficients in diagonal positions, which can be solved efficiently by preconditioned conjugate gradient method.

Remark 4. In our study, we consider the coupled system of the Navier-Stokes equations with two Cahn-Hilliard-type equations and the MCL. In the absence of surfactant and MCL, decoupled, linear, first-order energy stable schemes were developed for two-phase hydrodynamics with variable densities and viscosities based on stabilization technique [70]. However, the presence of MCL boundary conditions (13)–(15) would complicate the problem. To the best of the authors' knowledge, a decoupled linear energy stable scheme could only be constructed for the system with static contact angle condition [57] instead of (15). This difficulty may be solved using the recently developed technique of nonlocal auxiliary variables [71], in which auxiliary dynamics are derived and the resulting discretized schemes can guarantee the energy stability of an modified energy.

We solve the system under the assumption of three-dimensional axisymmetry with respect to the z-axis. We have the following cylindrical domain

$$\Omega = \{ (r,z) \mid 0 \le r \le R,\ 0 \le z \le L \}, \tag{73}$$

where R, L are dimensionless parameters. Here, $r = 0$ corresponds to the z-axis (the centerline), $z = 0$ is the solid wall Γ, where the GNBC is imposed. Correspondingly, $\mathbf{u} = (u_r, u_z)$, where u_r, u_z denote velocities along the r, z directions respectively. Now, we introduce the mathematical expressions for the gradient, divergence and Laplace operators in axisymmetric cylindrical coordinates:

$$\nabla = \left(\frac{\partial}{\partial r}, \frac{\partial}{\partial z} \right), \qquad \nabla \cdot \mathbf{u} = \frac{1}{r}\frac{\partial (r u_r)}{\partial r} + \frac{\partial u_z}{\partial z}, \qquad \Delta = \nabla \cdot \nabla = \frac{1}{r}\frac{\partial}{\partial r}\left(r \frac{\partial}{\partial r} \right) + \frac{\partial^2}{\partial z^2},$$

$$\nabla \cdot \left[\eta D(\mathbf{u}) \right] = \nabla \cdot \left[\eta \left(\nabla \mathbf{u} + (\nabla \mathbf{u})^\top \right) \right] = \begin{pmatrix} \frac{2}{r}\frac{\partial}{\partial r}\left(r\eta \frac{\partial u_r}{\partial r} \right) - \frac{\eta}{r^2}u_r + \frac{\partial}{\partial z}\left(\eta \frac{\partial u_r}{\partial z} \right) + \frac{\partial}{\partial z}\left(\eta \frac{\partial u_z}{\partial r} \right) \\ \frac{1}{r}\frac{\partial}{\partial r}\left(r\eta \frac{\partial u_r}{\partial z} \right) + \frac{1}{r}\frac{\partial}{\partial r}\left(r\eta \frac{\partial u_z}{\partial r} \right) + 2\frac{\partial}{\partial z}\left(\eta \frac{\partial u_z}{\partial z} \right) \end{pmatrix}.$$

Moreover, the GNBC (32)–(34) on Γ ($z = 0$) becomes

$$\frac{\phi^{n+1} - \phi^n}{\Delta t} + u_r^{n+1}\partial_r \phi^n = -\frac{1}{\mathrm{Pe}_s}L_\phi^{n+1}, \tag{74}$$

$$\frac{u_s^{n+1}}{\mathrm{L}_s l_s^{n+1}} = \frac{L_\phi^{n+1}\partial_r \phi^n}{\mathrm{Ca}\eta^{n+1}} - \partial_z u_r^{n+1}, \tag{75}$$

$$\partial_z \mu_\phi^{n+1} = 0, \qquad \mathrm{Pi}\partial_z \psi^{n+1} + M_\psi^n \partial_z \left(\frac{1}{2\mathrm{Ex}}(\phi^n)^2 - \frac{1}{4}\left((\phi^n)^2 - 1 \right)^2 \right) = 0, \qquad u_z^{n+1} = 0, \tag{76}$$

with

$$L_\phi^{n+1} = \mathrm{Cn}\partial_z \phi^{n+1} + s_2(\phi^{n+1} - \phi^n) + \gamma'_{wf}(\phi^n), \qquad u_s^{n+1} = u_r^{n+1} - u_w.$$

The remaining boundary conditions are also modified as follows:

$$\partial_z \phi^{n+1} = 0, \qquad \partial_z \mu_\phi^{n+1} = 0, \qquad \partial_z \psi^{n+1} = 0, \qquad \partial_z u_r^{n+1} = 0, \qquad u_z^{n+1} = 0 \qquad \text{on } z = L,$$

$$\partial_r \phi^{n+1} = 0, \qquad \partial_r \mu_\phi^{n+1} = 0, \qquad \partial_r \psi^{n+1} = 0, \qquad u_r^{n+1} = 0, \qquad \partial_r u_z^{n+1} = 0 \qquad \text{on } r = 0,$$

$$\partial_r \phi^{n+1} = 0, \qquad \partial_r \mu_\phi^{n+1} = 0, \qquad \partial_r \psi^{n+1} = 0, \qquad u_r^{n+1} = 0, \qquad \partial_r u_z^{n+1} = 0 \qquad \text{on } r = R.$$

Similarly, the second-order BDF scheme (58)–(72) can be rewritten accordingly. Furthermore, we will introduce the spatial discretization for these schemes in Appendix B.

We use efficient iterative methods to solve the resulting schemes, e.g., generalized minimal residual method (GMRES) with the Fast Fourier transform (FFT) [72] preconditioner under the periodic boundary conditions. It should be noted that due to Neumann

boundary conditions for ψ^{n+1} and p^{n+1}, we can accelerate the computation using discrete cosine transform in z-direction. Then their z-components can be decoupled in spectral space, and the resulting linear system in r-direction can be efficiently solved by direct elimination. This acceleration can be further improved when the system is solved in Cartesian coordinates, where ϕ^{n+1} can also be solved using FFT efficiently.

Remark 5. The presented schemes are applicable to the cases of high density ratios and viscosity ratios due to the use of the pressure stabilization method in Navier-Stokes equations. It is necessary to pay special attention to the discretization of convection terms for the high density ratio case. Third order weighted essentially non-oscillatory (WENO) schemes [73] could be used to reduce the undershoot and overshoot around the interface. Moreover, for the purpose of volume conservation in phase-field variable, the numerical truncation of ϕ will be also adopted, in which ϕ can be redistributed as follows [65]:

1. Truncate the undershoot/overshoot values:

$$\hat{\phi} = \begin{cases} 1 & \text{if } \phi > 1 + 10^{-7}, \\ -1 & \text{if } \phi < -(1 + 10^{-7}). \end{cases}$$

2. Compute the difference D of the two different total masses:

$$D = \int_\Omega \phi \mathrm{d}x - \int_\Omega \hat{\phi} \mathrm{d}x.$$

3. Uniformly distribute D at N_D points as D/N_D, where N_D is the total number of cells that fall into the interface region ($-0.999 < \phi < 0.999$).

However, in our simulations, this redistribution is not used due to low density ratio except for the last two examples in Sect. 4.3.4.

4. Numerical simulations

In this section, we will show several numerical experiments to validate the accuracy and stability of the proposed schemes, and study the influence of surfactants on the droplet impact dynamics. We first obtain the convergence rates of the proposed first-order and second-order schemes in Sect. 4.1. The property of energy decay of these schemes is numerically validated and the validity of the model is confirmed in Sect. 4.2. Then, in Sect. 4.3, we simulate droplets impacting on the solid surfaces with different values of Reynolds number, Weber number and Young's angle in two cases: one with a clean droplet and the other with a contaminated droplet by surfactants. Moreover, we compare our numerical results to the experimental results and observe qualitative agreement in Sect. 4.3.4, which gives a prediction of droplet impact dynamics with surfactants in real experiments.

Unless otherwise specified, the default values of some parameters are chosen as follows,

$$\text{Cn} = 0.01, \quad \text{Pe}_\phi = 100, \quad \text{Pe}_s = 0.002, \quad \text{Pi} = 0.1841,$$

$$\text{Ex} = 1, \quad \lambda_\rho = 0.1, \quad \lambda_\eta = 0.5, \quad \lambda_{l_s} = 1.$$

The computational domain Ω is determined by (73) with $R = L = 1$, i.e., $(r, z) \in [0, 1] \times [0, 1]$, except for Sect. 4.3.4, in which the domain is selected according to the real experiments. The grids is $(n_r, n_z) = (N, N)$ and $h = 1/N$ is the spatial resolution, where N is chosen appropriately for different sections. Different values of N and Δt are chosen for accuracy test in Sect. 4.1, whereas we use a uniform mesh with $h = 0.005$ and $\Delta t = 10^{-4}$ in Sect. 4.2–4.3. Moreover, we assume droplet impacts occur under the following conditions: (i) in axisymmetric motion; (ii) with non-ionic surfactant; (iii) with low surfactant concentration.

4.1. Accuracy test

In this section, we choose that

$$\text{Re} = 20, \quad \text{We} = 2, \quad \text{L}_s = 0.1, \quad \theta_s = 60°, \quad \text{Pe}_\psi = 10,$$

and set the following initial values:

$$\psi(r, z, t = 0) = 0.01,$$

$$\phi(r, z, t = 0) = \tanh\left(50\sqrt{2} \times (\sqrt{r^2 + z^2} - 0.5)\right),$$

$$\mathbf{u}(r, z, t = 0) = \mathbf{0}.$$

For the spatial convergence test, $N = 50, 100, 200, 400, 800$ are chosen and the numerical solutions are obtained by applying the first-order and second-order (in time) schemes at $t = 0.4$. We choose the solution on the finest mesh as the reference, and use $\Delta t = 10^{-5}$ for the temporal resolution so that the errors arising from the time discretization are negligible compared with the spatial errors. As shown in Table 1, for both schemes, the results demonstrate second order accuracy in space for all quantities ψ, ϕ and $\mathbf{u}$.

Table 1

Spatial errors and convergence rates for ψ, ϕ and **u** at $t = 0.4$ with fixed $\Delta t = 10^{-5}$ and different grids N. The errors are computed by comparing with the reference solution on the finest mesh with $N = 800$. $e(\cdot)$ is the error in l_2 norm.

	1st-order scheme							
N	$e(\psi)$	order	$e(\phi)$	order	$e(u_r)$	order	$e(u_z)$	order
50	5.10E−2	–	5.21E−2	–	3.58E−2	–	3.61E−2	–
100	1.38E−2	1.89	1.27E−2	2.04	9.01E−3	1.99	9.28E−3	1.96
200	3.32E−3	2.05	3.04E−3	2.06	2.03E−3	2.15	2.23E−3	2.06
400	7.70E−4	2.11	7.09E−4	2.10	4.54E−4	2.16	4.58E−4	2.28
	2nd-order scheme							
N	$e(\psi)$	order	$e(\phi)$	order	$e(u_r)$	order	$e(u_z)$	order
50	4.10E−2	–	4.61E−2	–	3.01E−2	–	3.04E−2	–
100	1.02E−2	2.01	1.11E−2	2.05	7.68E−3	1.97	7.65E−3	1.99
200	2.48E−3	2.04	2.53E−3	2.14	1.80E−3	2.09	1.81E−3	2.08
400	5.35E−4	2.21	6.27E−4	2.01	4.15E−4	2.12	3.97E−4	2.19

Table 2

Temporal errors and convergence rates for ψ, ϕ and **u** at $t = 0.4$ with different step sizes Δt. Corresponding spatial resolution $h = 2\Delta t$ with $h = 1/N$. The errors are computed by comparing with the reference solution obtained by the second-order scheme with $\Delta t = 10^{-4}$ and $h = 5 \times 10^{-4}$. $e(\cdot)$ is the error in l_2 norm.

	1st-order scheme							
Δt	$e(\psi)$	order	$e(\phi)$	order	$e(u_r)$	order	$e(u_z)$	order
1/200	3.56E−2	–	3.98E−2	–	2.51E−2	–	2.66E−2	–
1/400	1.84E−2	0.95	2.05E−2	0.96	1.26E−2	0.99	1.40E−2	0.93
1/800	7.96E−3	1.21	1.03E−2	0.99	5.94E−3	1.09	6.42E−3	1.12
1/1600	3.51E−3	1.18	4.84E−3	1.09	2.55E−3	1.22	2.68E−3	1.26
	2nd-order scheme							
Δt	$e(\psi)$	order	$e(\phi)$	order	$e(u_r)$	order	$e(u_z)$	order
1/200	1.19E−2	–	1.26E−2	–	9.37E−3	–	9.89E−3	–
1/400	3.21E−3	1.89	3.47E−3	1.86	2.49E−3	1.91	2.58E−3	1.94
1/800	7.86E−4	2.03	8.92E−4	1.96	6.19E−4	2.01	6.81E−4	1.92
1/1600	1.82E−4	2.11	2.14E−4	2.06	1.58E−4	1.97	1.73E−4	1.98

In the convergence test for temporal discretization, the numerical solutions are obtained by applying the first-order and second-order schemes with different time steps $\Delta t = 1/200, 1/400, 1/800, 1/1600$ at $t = 0.4$. For different Δt, the corresponding spatial resolution is $h = 2\Delta t$. The reference solution is obtained by applying the second-order scheme with $\Delta t = 10^{-4}$ and $h = 5 \times 10^{-4}$. As shown in Table 2, the schemes achieve first order and second order accuracy in time respectively.

Furthermore, to demonstrate the accuracy of the present schemes, we test the droplet dynamics in uniform flow and the error dependence of the divergence-free on various parameters, as shown in Appendix C.

4.2. Energy stability and model validation

In this section, the values of the parameters and the initial conditions are the same as Sect. 4.1, except that $\psi(r, z, t = 0) = 0.02 + 0.01\chi$, where χ is a random variable uniformly distributed in $[0, 1]$. We perform the computation until $t = 15$ so that the system almost reaches steady state.

Fig. 2a reveals that the total energies always decay with time for both first-order and second-order schemes, and the difference between them is almost negligible. In addition, the evolution curves of different parts in total energies are shown in Fig. 2b. It can be observed that the adsorption energy E_{ad} decreases with time, whereas the mixing entropy E_{sur} increases with time. This reveals the adsorption of surfactant onto the two-phase interface, which can also be observed in Fig. 3b. The Ginzburg-Landau energy E_{GL} increases and the wall energy E_{wf} decreases until stable states are achieved, indicating the dilation of two-phase interface and wetting area in wetting process. From the evolution of kinetic energy E_k, we know that the nonzero velocity field is generated at the beginning according to the initial contact line motion, and attenuates rapidly around about $t = 0.4$, after which the system achieves the quasi-static state. In summary, the interplay among interface evolution, surfactant diffusion, adsorption kinetic, and contact line dynamics become dominant in a long period until the system is near the equilibrium state.

For both hydrophilic ($\theta_s = 60°$) and hydrophobic ($\theta_s = 120°$) surfaces, two droplets (clean and contaminated) are selected for comparison to demonstrate the effect of surfactants on the dynamics of MCL. To see how the droplets and the surfactant evolve, the initial and steady states of the droplet profiles and surfactant distributions are shown in Fig. 3, which are computed by using the second-order scheme (58)–(72) until the steady state ($t = 15$). In Fig. 3b, the surfactant concentration around the interface is
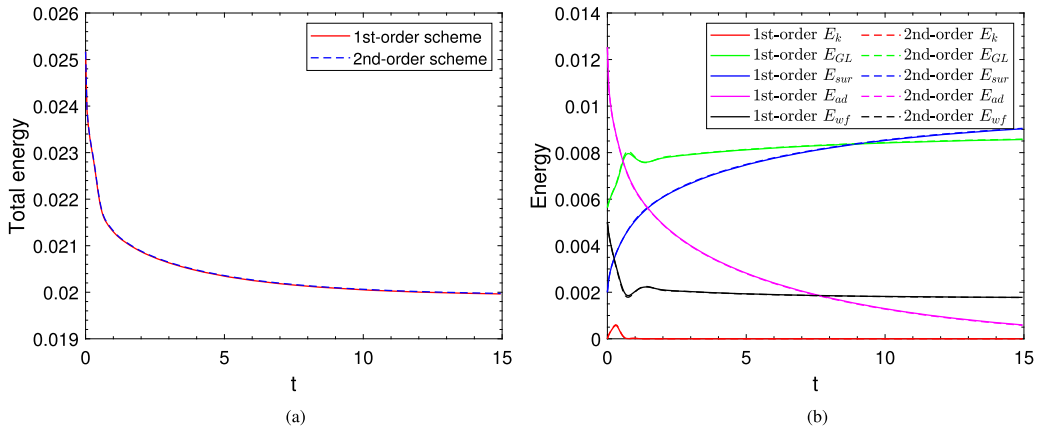
Fig. 2. Evolution of different types of energies obtained from first-order scheme (solid lines) and second-order scheme (dashed lines). (a) The total energy E_{tot}; (b) different parts in the total energy.
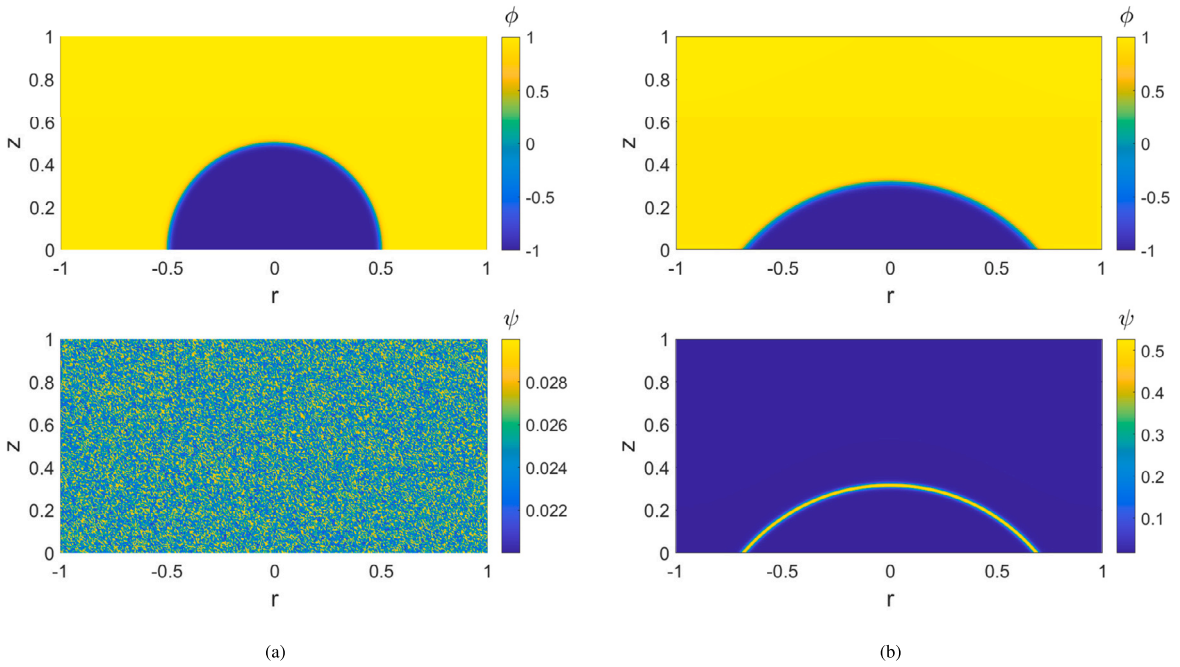

Fig. 3. Cross-sectional plots of (a) initial droplet profile (upper panel) and surfactant distribution (lower panel); (b) final droplet profile (upper panel) and surfactant distribution (lower panel). Hydrophilic surface ($\theta_s = 60°$) is considered. The final state is at $t = 15$.

obviously higher than that in other regions in equilibrium. The clean and contaminated droplets constantly spread or recoil until they reach their equilibrium states (shown in Fig. 4). Obviously, the presence of surfactant enhances hydrophilicity of a wetting droplet with its equilibrium contact angle decreasing to 47.1°, while it also helps droplet dewetting on hydrophobic surface with its equilibrium contact angle increasing to 132.2°. In a word, surfactants affect wetting properties (such as equilibrium contact angle, contact line velocity) by altering surface tensions. This leads to many real applications, for example, removing grease from clothing using detergents.

4.3. Droplet impact on a solid wall

In this section, we apply our second-order energy stable scheme (58)–(72) to simulate a droplet impacting on a solid surface. To demonstrate the influence of surfactants on the impact dynamics clearly, we compare the impact behaviors for clean and contaminated (with surfactants) droplets on hydrophilic and hydrophobic surfaces. Motivated by [61], we study the processes by varying Reynolds number, Weber number and wettability of the solid surface. Different choices of these parameters will result in different phenomena, including adherence, partial bouncing, bouncing and splashing. Moreover, we control diffusion and adsorption ability of surfactants by varying Pe_ψ. We show both three-dimensional plots of droplet profiles and their two-dimensional cross-sectional
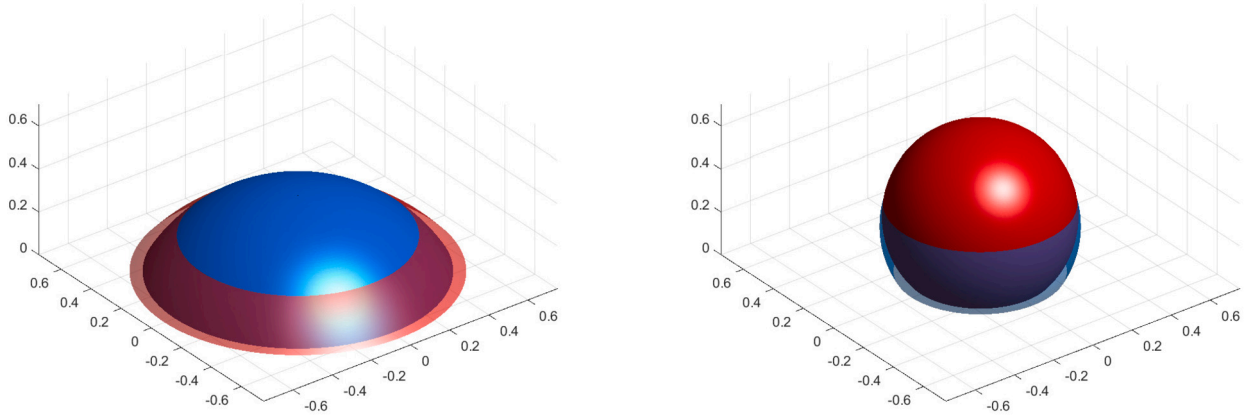
Fig. 4. Comparison of equilibrium profiles of clean (blue sphere) and contaminated (red sphere) droplets on different surfaces: (left panel) hydrophilic surface with $\theta_s = 60°$; (right panel) hydrophobic surface with $\theta_s = 120°$. For contaminated droplets, the initial surfactant concentrations are random in $(0.02, 0.03)$. In equilibrium, the contact angles of clean and contaminated droplets are respectively 59.3° and 47.1° for hydrophilic case, while they are respectively 120° and 132.2° for hydrophobic case.
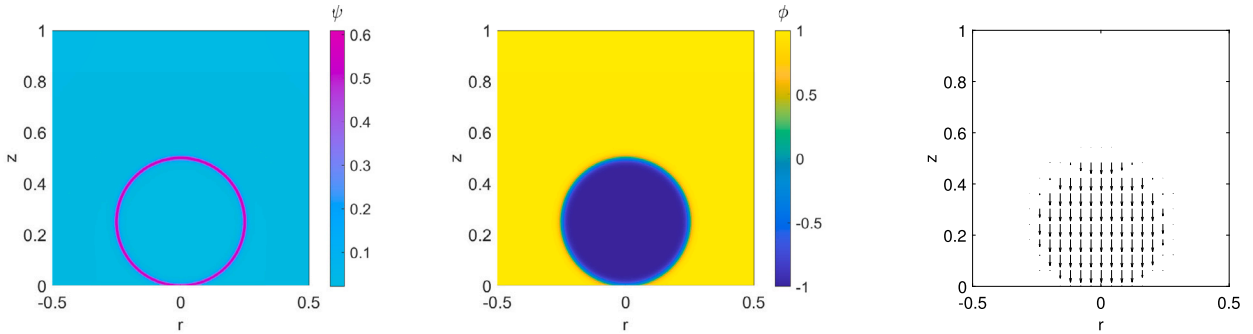
Fig. 5. From left to right, the initial profiles of ψ, ϕ and $\mathbf{u}$ in Examples 1–7 are shown.

plots in radial direction. To illustrate the dynamics of fluids and surfactants, we also show the velocity fields and the concentration distribution of surfactant in cross-sectional plots.

In all of the examples, a circular droplet with radius $r = 0.25$ initially located at $(0, 0.25)$ is considered in two cases: one clean and the other contaminated with soluble surfactant accumulated on the interface of droplet. Here, this contaminated droplet is generated by independently evolving (58) from an initial uniform surfactant distribution (with $\psi = 0.03$ everywhere) until steady state is reached, where ϕ is given in (77) indicating a circular shape and $\mathbf{u} = \mathbf{0}$ is fixed. At the beginning, we assign the droplets with a downward initial velocity of absolute value 1. In summary, the initial conditions are mathematically expressed as

$$\phi(r, z, t = 0) = \tanh\left(50\sqrt{2} \times \left(\sqrt{r^2 + (z - 0.25)^2} - 0.25\right)\right), \tag{77}$$

$$u_r(r, z, t = 0) = 0, \qquad u_z(r, z, t = 0) = -0.5 \times \left(1 - \tanh\left(50\sqrt{2} \times \left(\sqrt{r^2 + (z - 0.25)^2} - 0.25\right)\right)\right), \tag{78}$$

and their profiles are shown in Fig. 5. To be more precise, we set the initial velocity field that is smoothed from (78) and is nearly divergence-free. Initially, the surfactant concentrates on the interface and is uniformly distributed along its perimeter. Moreover, we fix the parameter $L_s = 0.0025$ in Examples 1–5, while L_s is chosen accordingly in Examples 6 and 7 in order to fit the experimental phenomena. The values of Re, We, θ_s and Pe_ψ will be specified below.

4.3.1. Adherence

In this section, we consider the first two examples for droplet adherence, which will happen when the initial kinetic energy is not large and the dissipation is large. In second example shown below, when surfactants are present, the outcome of the impact transits from adherence to complete bouncing.

Example 1. In this example, we choose the following parameters for the simulation:

$$Re = 800, \qquad We = 245.1, \qquad \theta_s = 90°, \qquad Pe_\psi = 100.$$

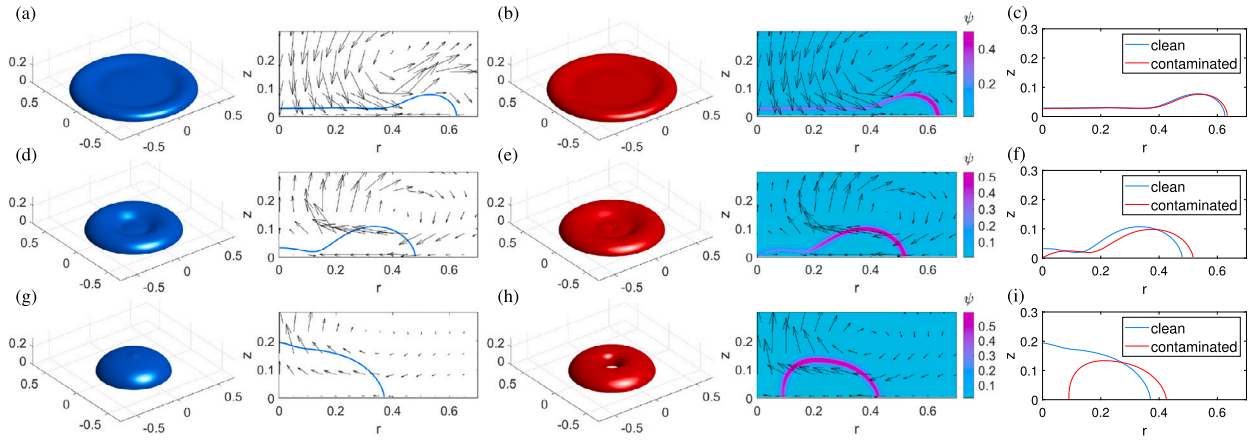The evolutional profiles of droplet and surfactant concentration are depicted in Fig. 6.

Fig. 6. Droplet adherence in Example 1 (Re = 800, We = 245.1, $\theta_s = 90°$, and $Pe_\psi = 100$). Profiles of clean and contaminated droplets are shown in both three-dimensional views (1st and 3rd columns) and two-dimensional radial plots (2nd and 4th columns). Velocity fields and surfactant concentrations are also shown in the radial plots by quivers and colormaps respectively. Comparisons between the interface shapes of clean and contaminated droplets are given in the 5th column. Snapshots are captured at time $t = 1.6$ (a–c), $t = 3.08$ (d–f), and $t = 4$ (g–i).

As shown in Fig. 6a–c, both the clean and contaminated droplets behave in similar manners at the beginning ($t = 1.6$). Due to contact line dynamics and the flow nearby the interface, the surfactant on the contaminated droplet concentrates at the moving front, leading to a lower surface tension. This lower surface tension makes the moving front of interface deformed more easily, which results in a smaller contact angle than that of the clean droplet. By uncompensated Young stress, smaller contact angle (and thus larger deviation from Young's angle) gives rise to larger contact line speed. Therefore, the contact line dynamics is accelerated and the front moves faster in the contaminated droplet. Moreover, the non-uniform distribution in surfactant concentration induces a gradient in surface tension and generates Marangoni force, which also contributes to the spreading dynamics.

When the droplets attain their maximal radii, they lose most of their kinetic energies while they store a large amount of surface energies. Then they start to release these surface energies through recoiling towards their centers. However, since surface tension is reduced due to the addition of surfactant, the contaminated droplet is more easily deformed and its center part becomes thinner than that of the clean droplet, which gives rise to breakup tendency as shown in Fig. 6d–f. When the contaminated droplet breaks up from the center, a new contact line forms and recedes outwards as a result of uncompensated Young stress (Fig. 6h). The droplet behaves as a doughnut-like torus with shrinking width. In comparison, the clean droplet continues to recoil towards a spherical shape (Fig. 6g) and the difference between its shape and that of the contaminated one at $t = 4$ is shown in Fig. 6i. The torus shape of the contaminated droplet does not last long due to surface tension, it continues evolving until a spherical shape is achieved in the end.

In this example, both the clean and contaminated droplets adhere on the substrate. The contaminated droplet experiences topological changes while the clean one does not. The differences between the two processes can also be read from the plots of dissipations. As illustrated in Fig. 7, both viscous (R_v) and slip (R_s) dissipations decay after initial peaks during droplet impact. They dominate the other dissipations and gently vary in spreading dynamics. In the spreading stage, the diffusion (R_d) and relaxation (R_r) dissipations become important in the sense of encoding interfacial evolution and identifying topological changes, although they are not large in magnitude. For instance, when topological change happens around $t = 3.08$ and a 'contaminated' torus forms, an increasing in R_d (and also in R_r) is observed (dashed pink curve in the inset plot of Fig. 7a). Therefore, we can easily distinguish the contaminated case from the clean case by simply looking at these two dissipations. In addition, some particular interface profiles can also be reflected when these two dissipations experience rapid changes (See Fig. 7b and 7c).

Example 2. In this example, we strengthen both inertial and capillary effects by increasing Reynold number and decreasing Weber number as follows:

$$Re = 1600, \qquad We = 18.9, \qquad \theta_s = 90°, \qquad Pe_\psi = 10,$$

where Péclet number is taken to be smaller for the purpose of improving surfactant effect by enhancing adsorption.

Similar as in Example 1, after the initial impact, both clean and contaminated droplets spread until they achieve their maximal radii. This is followed by droplet recoiling during which topological changes occur in both cases and a hole generates in the center (Fig. 8a–c). There is a slight difference that in the contaminated case a new island forms in the center. This may be attributed to the lower surface tension caused by surfactant, which makes the interface more easily deformed and the contaminated droplet 'softer'.

Due to large inertial effect, the droplet brings a lot of kinetic energy (more than that in Example 1) and would bounce. However, the large capillary force makes the droplet stiffer and less deformed. As a result, the clean droplet is 'dragged' and does not bounce. The balance between capillary and inertial effects leads to an oscillatory motion with amplitude decreasing in time (Fig. 8d,g). In contrast, in the contaminated case, the presence of surfactant weakens capillary force and makes the droplet 'softer'. As a result of droplet deformation, the upward velocity field generates nearby the interface, which provides a lifting flow driving the droplet off entirely from the solid surface at time $t = 3.3$ (Fig. 8e,h). A detailed comparison in the interface shapes is also given in Fig. 8f,i.
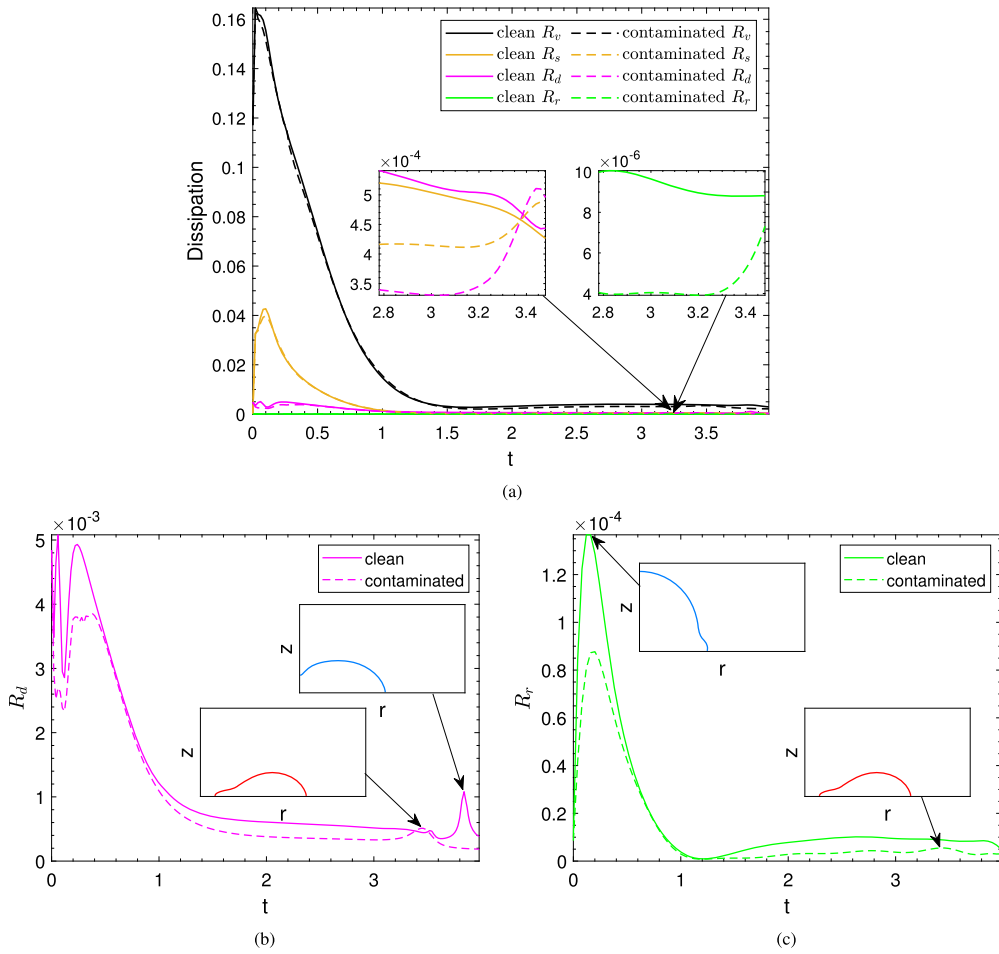
Fig. 7. Dissipations in Example 1. In (a), four dissipations are shown for both clean (solid curves) and contaminated (dashed curves) cases, including viscous dissipation R_v, slip dissipation R_s, diffusion dissipation R_d, and relaxation dissipation R_r. The inset plots illustrate differences in dissipations for the two cases when topological change occurs. In particular, R_d and R_r are shown in (b) and (c), where their rapid changes indicate some particular interface geometries in the inset plots.

Again, rapid changes (and peaks) in dissipations indicate topological changes, such as formation of torus and island, and droplet bouncing away from the substrate (Fig. 9). Moreover, it is also observed that each dissipation in the contaminated case is overall smaller than the corresponding one in the clean case. This explains why the contaminated droplet can bounce while the clean one cannot.

4.3.2. Bouncing

In this section, we numerically investigate bouncing phenomena.

Example 3. In comparison to Example 2, we enlarge the Weber number so that the capillary effect is weakened. The following parameters are taken:

$$\text{Re} = 1600, \qquad \text{We} = 37.7, \qquad \theta_s = 90°, \qquad \text{Pe}_\psi = 10.$$

As shown in Fig. 10a–c, the spreading dynamics in both cases are similar as in Example 2. However, due to the weakened capillary effect, both the clean and contaminated droplets are able to bounce (Fig. 10d–i). The contaminated droplet is 'softer' so that in bouncing process it breaks up into two parts: one continues to rise, while the other stays on the substrate. This leads to partial bouncing (Fig. 10h). In contrast, the clean droplet experiences complete bouncing (Fig. 10g).

In Fig. 11, more peaks in dissipations are observed, indicating complex topological changes happen. In particular, breakup in the bouncing contaminated droplet occurs nearby the peak in R_d around $t = 4.71$, meanwhile, the clean droplet has completely left the substrate since the peak in R_d emerges around $t = 3.87$.

Example 4. Droplet bouncing is more easily to happen if we further enlarge the Weber number while making the substrate hydrophobic. In particular, we choose the following parameters:
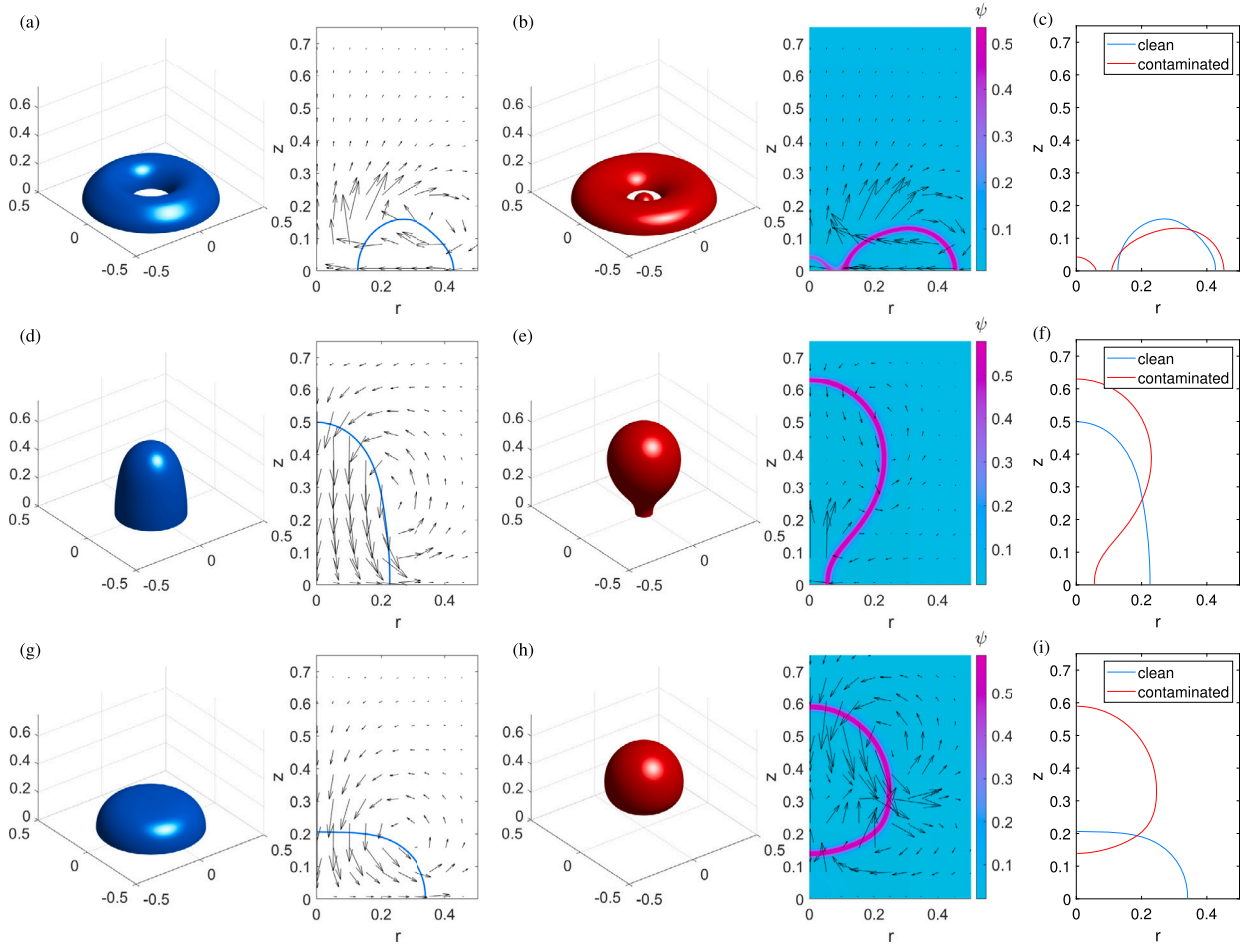
Fig. 8. Droplet adherence and bouncing in Example 2 (Re = 1600, We = 18.9, $\theta_s = 90°$, and $Pe_\psi = 10$). Profiles of clean and contaminated droplets are shown in both three-dimensional views (1st and 3rd columns) and two-dimensional radial plots (2nd and 4th columns). Velocity fields and surfactant concentrations are also shown in the radial plots by quivers and colormaps respectively. Comparisons between the interface shapes of clean and contaminated droplets are given in the 5th column. Snapshots are captured at time $t = 0.9$ (a–c), $t = 2.88$ (d–f), and $t = 3.3$ (g–i).

$$\text{Re} = 2000, \qquad \text{We} = 282.8, \qquad \theta_s = 100°, \qquad \text{Pe}_\psi = 100.$$

In this case, both clean and contaminated droplets undergo complete bouncing. As shown in Fig. 12a–c, breakups are more easily to happen in the spreading dynamics of the contaminated droplet. In recoiling process, the central component of droplet first bounces, while it takes some time for the peripheric component (torus part) to agglomerate and then bounce. It can be observed in Fig. 12d–i that in both clean and contaminated cases, two small drops rise with the lower one chasing the upper one until they merge. Due to the presence of surfactant, the two contaminated drops are more likely to be deformed and keep in contact without merging. It takes longer time for them to merge compared to the clean case.

In the plots of dissipations (Fig. 13), one can infer more topological changes by examining peaks in R_d and R_r. In addition, merging of two drops can also be inferred from the rapid change of R_d around $t = 8$ and $t = 10.8$.

4.3.3. Splashing

When the substrate is more hydrophobic so that it becomes less stick, droplet splashing will happen.

Example 5. We investigate splashing using the following parameters:

$$\text{Re} = 1600, \qquad \text{We} = 282.8, \qquad \theta_s = 160°, \qquad \text{Pe}_\psi = 100.$$

After droplet impact, the spreading dynamics follows. However, since the substrate is less sticky, the droplet does not recoil in a whole. Instead, the moving front of droplet upwarps its head, like a spindrift (Fig. 14a–c). As inertial effect is more important than capillary effect [58] at the moving front, breakup occurs and the head of the moving front takes off and leaves the substrate (Fig. 14d–f). In other words, splashing happens. The presence of surfactant makes the interface softer and break up into more flying
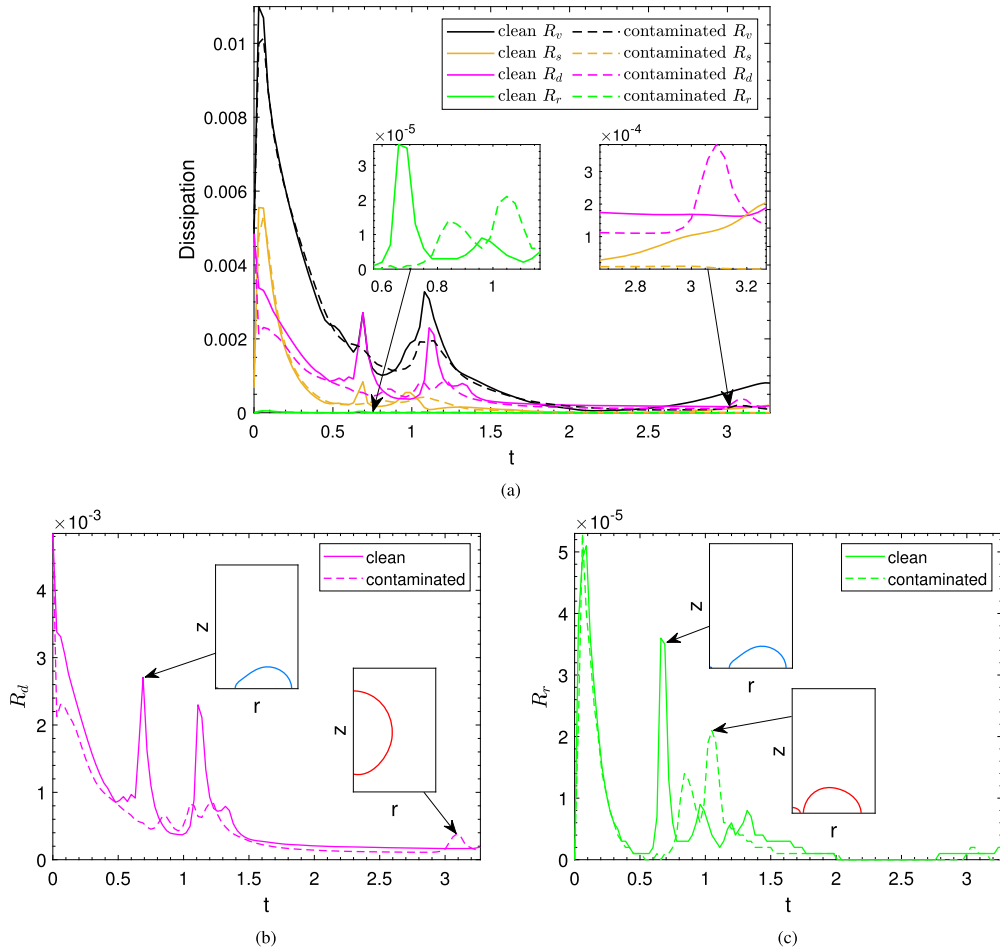
Fig. 9. Dissipations in Example 2. In (a), four dissipations are shown for both clean (solid curves) and contaminated (dashed curves) cases. The inset plots illustrate differences in dissipations for the two cases nearby topological changes (formation of torus and island, and droplet bouncing). In particular, R_d and R_r are shown in (b) and (c), where their peaks reflect some particular interface geometries in the inset plots.

drops (Fig. 14g–i). This is consistent with our understanding on surfactants, which make the droplet more "active" to the forcing movement and thus help dewetting.

As in previous examples, the dissipations in the contaminated case are in general smaller than that in the clean case (see Fig. 15), which implies that more free energy is carried by the contaminated droplet. This additional free energy is either transformed into kinetic energy or stored on complex interfaces with larger total area. As a consequence, breakups of droplet and bouncing (or splashing) are more likely to happen.

4.3.4. Comparison with experimental results

Experiments on droplet impact have been carried out in many literatures. For instance, [59] systematically studied adherence, bouncing, and partial bouncing of clean drops in their experiments. In this section, we apply our model and numerical methods to reproduce some of their experimental results. For comparison, we also make numerical predictions of impact behaviors for contaminated droplets under the same physical parameters.

Example 6. We study bouncing dynamics in this example. The same parameters as in the experiment are used, which after scaling are equivalent to

$$\text{Re} = 6490, \qquad \text{We} = 98, \qquad \text{L}_s = 0.0025, \qquad \theta_s = 95°, \qquad \lambda_\rho = \frac{1}{830}, \qquad \lambda_\eta = \frac{1}{66.2}.$$

In addition, we choose $\text{Pe}_\psi = 100$ for contaminated droplet in order to see the surfactant transport during impact dynamics. The computational domain is fixed to be $\Omega = [0, 1.5] \times [0, 2]$.

Experimental and numerical results for clean droplets are compared in Fig. 16. We see qualitative agreement between these two sets of results in spreading, recoiling and bouncing processes. In the recoiling stage (Fig. 16h,i), capillary wave instability results in ruptures of the thin film, creating a ring structure with dried out regions. The emergence of a ring structure with a dry-out region
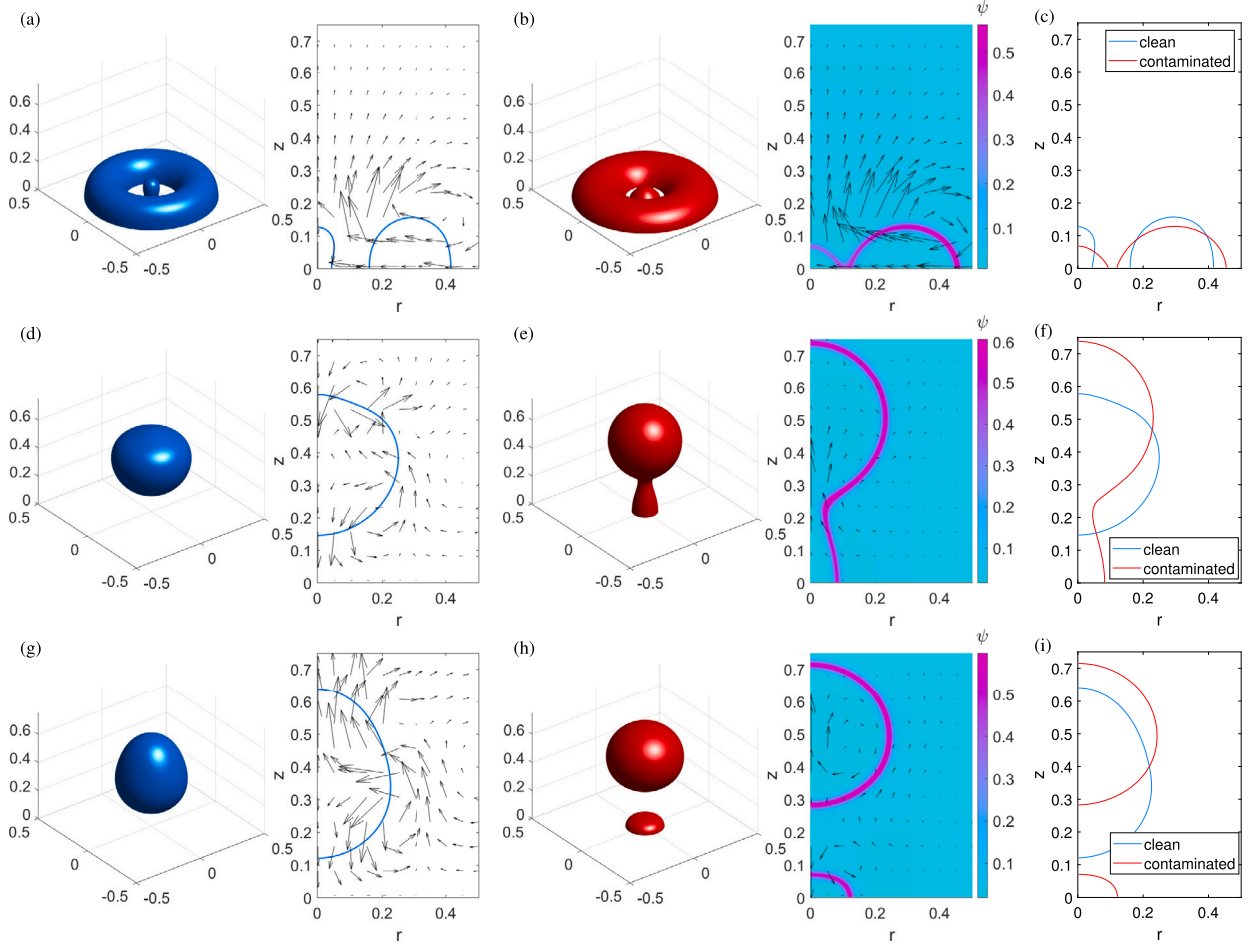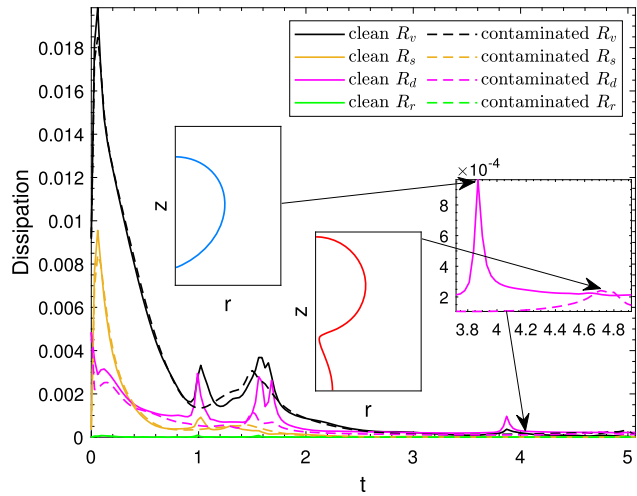
Fig. 10. Droplet bouncing and partial bouncing in Example 3 (Re = 1600, We = 37.7, $\theta_s = 90°$, and Pe$_\psi$ = 10). Profiles of clean and contaminated droplets are shown in both three-dimensional views (1st and 3rd columns) and two-dimensional radial plots (2nd and 4th columns). Velocity fields and surfactant concentrations are also shown in the radial plots by quivers and colormaps respectively. Comparisons between the interface shapes of clean and contaminated droplets are given in the 5th column. Snapshots are captured at time $t = 1.38$ (a–c), $t = 4.5$ (d–f), and $t = 5.1$ (g–i).

Fig. 11. Dissipations in Example 3. In (a), four dissipations are shown for both clean (solid curves) and contaminated (dashed curves) cases. The right inset plot illustrates differences in R_d for the two cases when topological change occurs, and some particular interface geometries corresponding to peaks of R_d are shown in other inset plots.
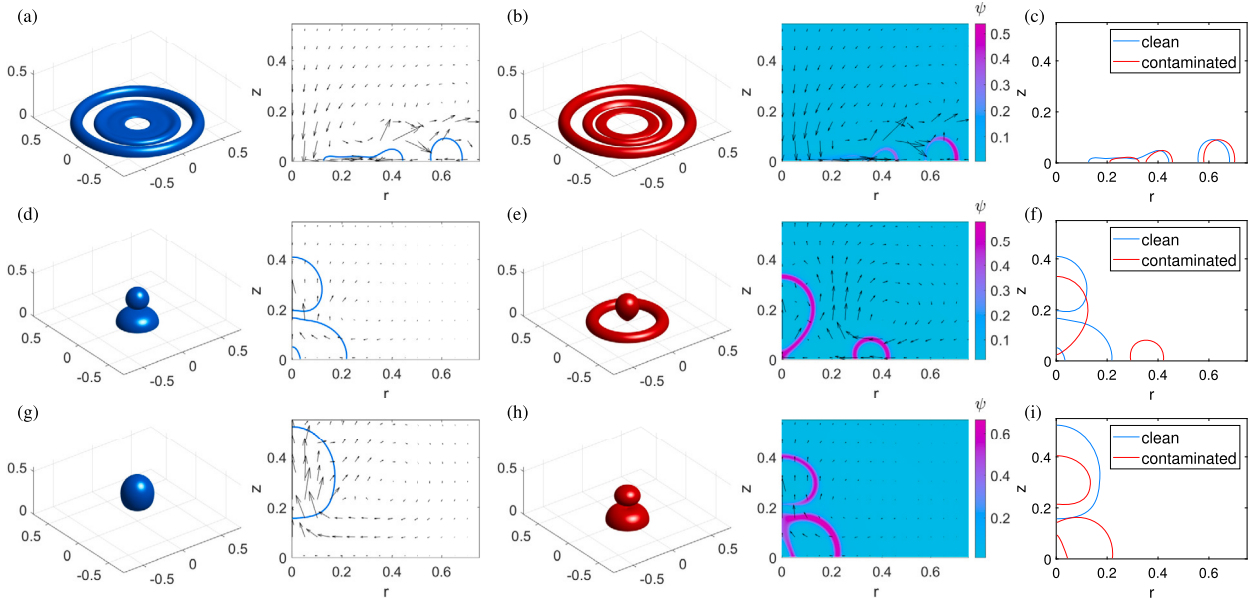
Fig. 12. Droplet bouncing in Example 4 (Re = 2000, We = 282.8, $\theta_s = 100°$, and Pe$_\psi$ = 100). Profiles of clean and contaminated droplets are shown in both three-dimensional views (1st and 3rd columns) and two-dimensional radial plots (2nd and 4th columns). Velocity fields and surfactant concentrations are also shown in the radial plots by quivers and colormaps respectively. Comparisons between the interface shapes of clean and contaminated droplets are given in the 5th column. Snapshots are captured at time $t = 2.04$ (a–c), $t = 7.92$ (d–f), and $t = 10.64$ (g–i).
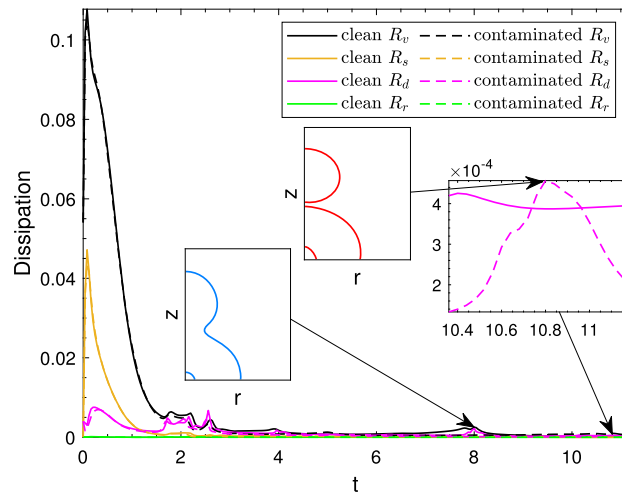

Fig. 13. Dissipations in Example 4. In (a), four dissipations are shown for both clean (solid curves) and contaminated (dashed curves) cases. The right inset plot illustrates differences in R_d for the two cases when topological change occurs, and some particular interface geometries corresponding to some of peaks are shown in other inset plots.

for large enough Re and We was also reported experimentally and numerically in [60]. In Fig. 16n,q, the rising droplet breaks up into two parts, with one part staying on the surface and the other flying in the air. This leads to the result of partial bouncing for the clean droplet.

When surfactant is present, it gradually migrates from the center part of interface towards moving front (Fig. 16c,f) as a result of convection and diffusion (Marangoni effect also helps). When recoiling, the contaminated droplet breaks up into three tori in comparison to the clean case (Fig. 16i). The hole in the center continues to exist even in the bouncing process (Fig. 16l,o). Breakup also occurs in the rising droplet, but with both child drops flying in the air. This phenomenon can also be attributed to the lower dissipations in impact dynamics of contaminated droplet, as we explained in Example 5.

Example 7. In this example, we investigate adherence phenomena for droplet impacting on a smooth glass plate (hydrophilic substrate). We also use the same parameters as in the experiment, which are given as
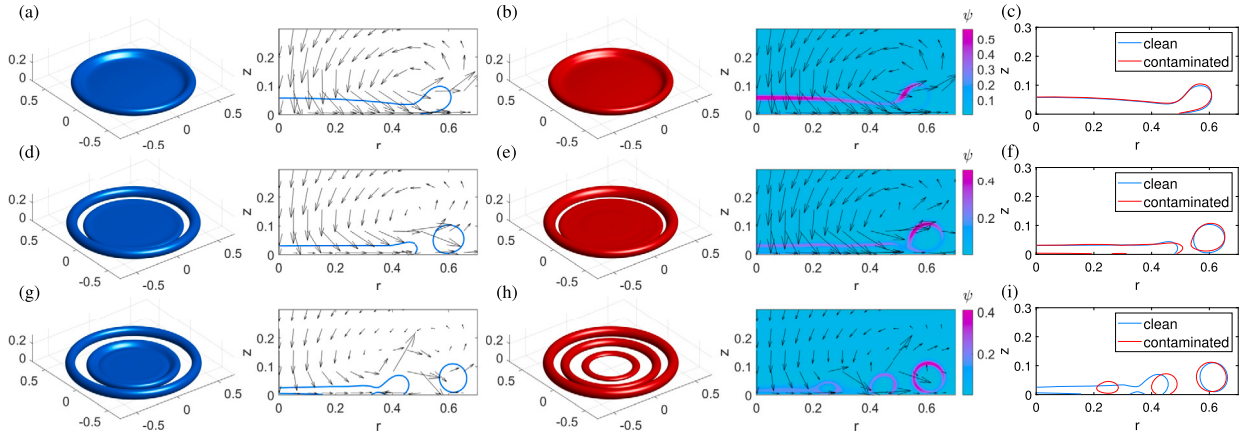
Fig. 14. Droplet splashing in Example 5 (Re = 1600, We = 282.8, $\theta_s = 160°$, and Pe$_\psi$ = 100). Profiles of clean and contaminated droplets are shown in both three-dimensional views (1st and 3rd columns) and two-dimensional radial plots (2nd and 4th columns). Velocity fields and surfactant concentrations are also shown in the radial plots by quivers and colormaps respectively. Comparisons between the interface shapes of clean and contaminated droplets are given in the 5th column. Snapshots are captured at time $t = 0.8$ (a–c), $t = 1.22$ (d–f), and $t = 1.48$ (g–i).
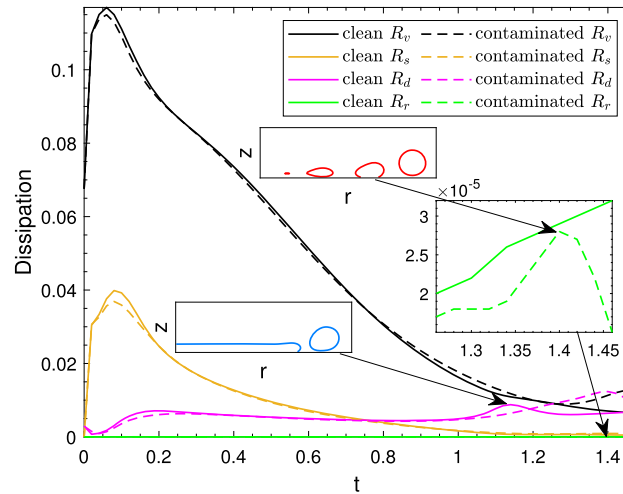

Fig. 15. Dissipations in Example 5. In (a), four dissipations are shown for both clean (solid curves) and contaminated (dashed curves) cases. The right inset plot illustrates differences in R_r for the two cases when topological change occurs, and some particular interface geometries corresponding to some of peaks are shown in other inset plots.

$$Re = 7174.4, \qquad We = 109.4, \qquad L_s = 10^{-6}, \qquad \theta_s = 10°, \qquad \lambda_\rho = \frac{1}{830}, \qquad \lambda_\eta = \frac{1}{66.2}.$$

Besides, we take Pe$_\psi$ = 60, Pe$_s$ = 0.5 and $\Omega = [0, 2] \times [0, 1]$.

The comparison between experimental and numerical results for clean droplet are shown in Fig. 17. Again, qualitative agreement between the two sets of results is observed. Different from all previous examples, the droplet keeps on spreading after its impact on the substrate until equilibrium profile is achieved. The major reason for this dynamics is that the substrate is very 'sticky' due to the very small Young's angle $\theta_s = 10°$. The contact line keeps on advancing until the contact angle achieves Young's angle. The initial kinetic energy is transformed to the surface energy of the droplet interface and the substrate.

The presence of surfactant does not change the impact and spreading dynamics too much. Surfactant transport also takes place from the center of interface towards the moving edge (Fig. 17c–l). The accumulation of surfactant at the moving edge reduces the interfacial tension near the contact line, giving rise to larger uncompensated Young stress and thus faster contact line dynamics (Fig. 17o–u). Eventually, a smaller equilibrium contact angle (than θ_s) is achieved. This phenomenon is also consistent with the simulation result on spreading dynamics (Fig. 4) in Sect. 4.2.

5. Conclusion

We considered two-phase flow problems with moving contact lines in the presence of surfactants, which were modeled by the NS-PFS-MCL system with variable density and viscosity. Based on convex splitting and pressure stabilization techniques, energy stable
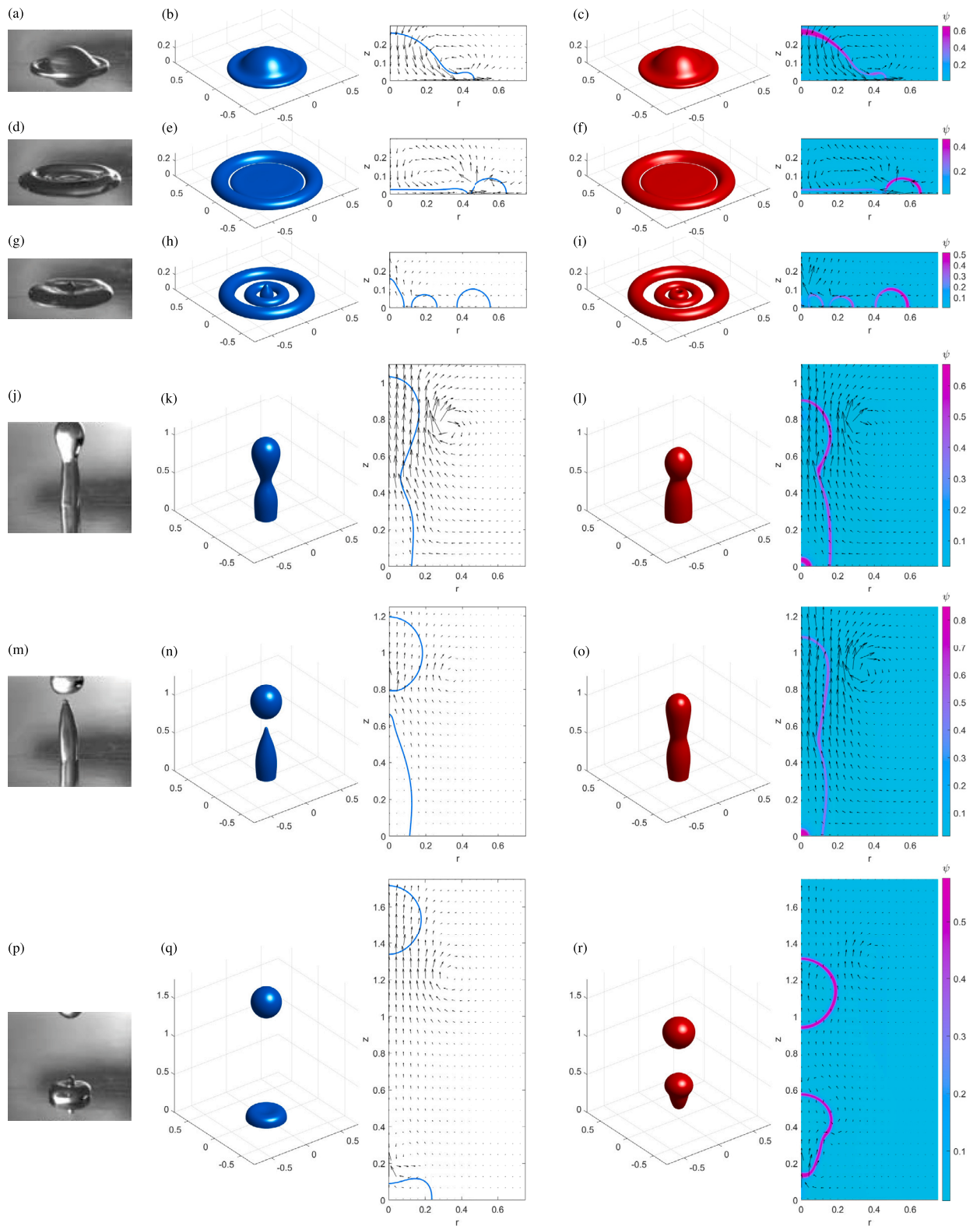
Fig. 16. Comparison with experimental results in Example 6: experimental and numerical results for dynamic process at time $t = 1.31$ ms (a), $t = 1.31$ ms (b, c); $t = 6.02$ ms (d), $t = 6.05$ ms (e, f); $t = 8.21$ ms (g), $t = 8.38$ ms (h, i); $t = 20.54$ ms (j), $t = 20.51$ ms (k, l); $t = 25.58$ ms (m), $t = 23.96$ ms (n, o); $t = 35.17$ ms (p), $t = 33.42$ ms (q, r). Experiment figures courtesy of [59].
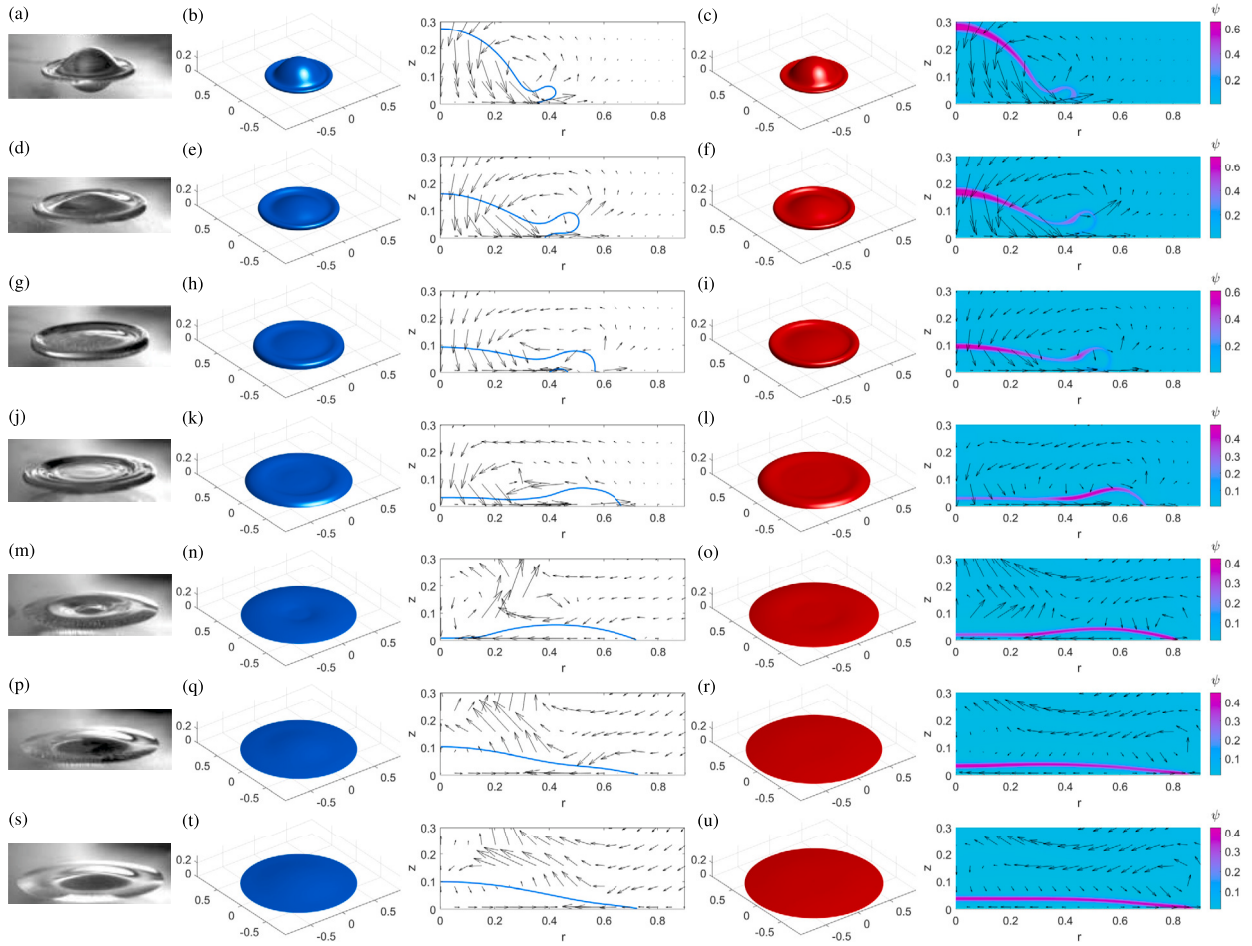
Fig. 17. Comparison with experimental results in Example 7: experimental and numerical results for dynamic process at time $t = 1.31$ ms (a), $t = 1.33$ ms (b, c); $t = 2.27$ ms (d), $t = 2.27$ ms (e, f); $t = 3.16$ ms (g), $t = 3.10$ ms (h, i); $t = 6.04$ ms (j), $t = 6.08$ ms (k, l); $t = 14.03$ ms (m), $t = 14.02$ ms (n, o); $t = 25.58$ ms (p), $t = 25.56$ ms (q, r); $t = 29.26$ ms (s), $t = 29.26$ ms (t, u). Experiment figures courtesy of [59].

methods were proposed for this model. In particular, we rigorously proved that the proposed first-order scheme is unconditionally energy stable without modifying the original energy. Moreover, we generalized the methods to be second-order accurate in the form of BDF scheme. The resulting schemes were implemented using linearization techniques in cylindrical coordinates with axisymmetry.

Numerical results were presented to validate accuracy and energy stability of the proposed schemes. We also systematically studied how surfactants affect contact line dynamics, especially in droplet impact. It was observed that the presence of surfactants makes the droplet more hydrophilic/hydrophobic on hydrophilic/hydrophobic surfaces. As a result, adding surfactants into an impact droplet can strengthen the adherence effect on hydrophilic surfaces (Example 7) while making splashing more severe on hydrophobic surfaces (Example 5). In general, the dissipation in the impact dynamics of a contaminated drop is smaller than that in the clean case, and topological changes are more likely to occur for contaminated drops. Moreover, adding surfactants may induce some qualitative changes in the droplet impact dynamics: A clean adherent droplet could experience complete bouncing when surfactants are added (Example 2); a clean droplet which completely rebounds becomes partially bounced in the presence of surfactants (Example 3). Lastly, we obtained qualitative agreements with experimental results for impact dynamics in the case without surfactants, and simulated impact processes for contaminated drops as comparisons.

Building linear and fully decoupled schemes satisfying unconditional energy stability with respect to original energy is still open due to the difficulty arising from potential singularity, nonlinear couplings, variable densities and the existence of the MCL. In addition, establishing bound-preserving property for both surfactant concentration ψ and phase-field variable ϕ is another challenging issue in numerical analysis and should be taken into account in consideration of real problems. Besides, for the purpose of maintaining divergence-free condition in two-phase flow with variable density, the continuity equation is modified in the proposed model in this work. This drawback can be remedied by considering the quasi-incompressible CHNS model [74,75], which can be potentially generalized to the study of the droplet impact with surfactants. Dependence of impact phenomena (adherence, bouncing or splashing) on dimensionless parameters, such as Re, We, θ_s and Pe$_\psi$, is also of great interest in realistic applications. This together with real three-dimensional simulations will be our future concern.

CRediT authorship contribution statement

Chenxi Wang: Software, Analysis, Writing - Original Draft.
Ming-Chih Lai: Writing - Review & Editing, Supervision.
Zhen Zhang: Conceptualization, Writing - Original Draft, Supervision.

Declaration of competing interest

The authors declare that they have no known competing financial interests or personal relationships that could have appeared to influence the work reported in this paper.

Data availability

No data was used for the research described in the article.

Acknowledgements

Appendix A. Non-dimensionalization

In this section, we will discuss the non-dimensionalization of the binary fluid phase-field surfactant model with the MCL. The free energy of the phase-field surfactant model described in [49] and the standard kinetic energy are utilized in our study:

$$E_{tot}(\mathbf{u}, \phi, \psi) = E_k(\mathbf{u}) + E_{GL}(\phi) + E_{sur}(\psi) + E_{ad}(\phi, \psi) + E_{wf}(\phi),$$

where

$$E_k(\mathbf{u}) = \int_\Omega \frac{\rho}{2} |\mathbf{u}|^2 \mathrm{d}x \quad \text{with} \quad \rho = \frac{\rho_2 - \rho_1}{2}\phi + \frac{\rho_1 + \rho_2}{2},$$

$$E_{GL}(\phi) = \int_\Omega \frac{\kappa}{2}|\nabla\phi|^2 - \frac{A}{2}\phi^2 + \frac{A}{4}\phi^4 + \frac{A}{4}\mathrm{d}x, \qquad E_{sur}(\psi) = \int_\Omega k_b T[\psi\ln\psi + (1-\psi)\ln(1-\psi)]\mathrm{d}x,$$

$$E_{ad}(\phi, \psi) = \int_\Omega \frac{W}{2}\psi\phi^2 - \frac{\varsigma}{4}\psi\left(1-\phi^2\right)^2 \mathrm{d}x, \qquad E_{wf}(\phi) = \int_\Gamma -\frac{\gamma}{2}\cos\theta_s \sin\left(\frac{\pi\phi}{2}\right) + \frac{\gamma_1 + \gamma_2}{2}\mathrm{d}S.$$

Here, ρ represents the density, κ and A are two phenomenological parameters. They are related to the interface profile thickness $\varepsilon = \sqrt{\kappa/A}$, the equilibrium phases $\phi_\pm = \pm 1$, and the interfacial tension $\gamma = 2\sqrt{2\kappa A}/3$. Additionally, k_b is the Boltzmann constant, T is the temperature, and W and ς are two positive parameters which describe the adsorption strength of surfactant on the interface. It is important to note that in this formulation, we implicitly assume $\varsigma = A$ in order to reduce unnecessary free parameters.

Next, we present the dissipations associated with the two-phase system with MCL and soluble surfactants:

$$R_v = \int_\Omega \frac{\eta}{2}\left\|D(\mathbf{u})\right\|_F^2 \mathrm{d}x, \qquad R_d = \int_\Omega \frac{J_\phi^2}{m_\phi}\mathrm{d}x, \qquad R_e = \int_\Omega \frac{J_\psi^2}{m_\psi M_\psi}\mathrm{d}x, \qquad R_r = \int_\Gamma \frac{\dot\phi^2}{m_\Gamma}\mathrm{d}S, \qquad R_s = \int_\Gamma \beta\mathbf{u}_s^2\mathrm{d}S,$$

where J_ϕ and J_ψ represent the diffusive fluxes resulting from composition diffusion and surfactant diffusion, respectively. m_ϕ, m_ψ and m_Γ are phenomenological mobility parameters. Denoting the viscosity and the slip coefficient of the system by η and β respectively, we have

$$\eta = \frac{\eta_2 - \eta_1}{2}\phi + \frac{\eta_1 + \eta_2}{2}, \qquad \beta = \frac{\beta_2 - \beta_1}{2}\phi + \frac{\beta_1 + \beta_2}{2}, \qquad \dot\phi = \phi_t + \mathbf{u}_\tau \cdot \nabla_\tau \phi.$$

These dissipations can be interpreted as follows: R_v represents the dissipation arising from viscous effects, R_d corresponds to the dissipation due to diffusion in phase-field dynamics, R_e is the dissipation resulting from diffusion in surfactant dynamics, R_r is the dissipation resulting from diffusion in surfactant dynamics, and R_s represents the dissipation due to slip. Based on the first law of thermodynamics (or equivalently the Onsager variational principle), the NS-PFS-MCL system can be derived [49].

Now, we can define the following dimensionless parameters:

$$\mathrm{Pe}_\phi = \frac{L_c U_c}{m_\phi A}, \quad \mathrm{Pe}_\psi = \frac{L_c U_c}{m_\psi A}, \quad \mathrm{Pe}_s = \frac{\varepsilon U_c}{\kappa m_\Gamma L_c}, \quad \mathrm{Ex} = \frac{\kappa}{W\varepsilon^2}, \quad \mathrm{Pi} = \frac{k_b T}{A}, \quad \mathrm{Cn} = \frac{\varepsilon}{L_c},$$

$$\mathrm{Re} = \frac{\rho_1 L_c U_c}{\eta_1}, \quad \mathrm{Ca} = \frac{2\sqrt{2}\eta_1 U_c}{3\gamma}, \quad \mathrm{We} = \mathrm{ReCa}, \quad L_s = \frac{\eta_1}{\beta_1 L_c}, \quad \lambda_\rho = \frac{\rho_2}{\rho_1}, \quad \lambda_\eta = \frac{\eta_2}{\eta_1}, \quad \lambda_{l_s} = \frac{\eta_2 \beta_1}{\eta_1 \beta_2},$$

where L_c is the characteristic length, U_c is the characteristic velocity. After scaling the energies and dissipations by AL_c^d and $AU_c L_c^{d-1}$ respectively, where d is the spatial dimension, we can obtain the dimensionless forms in Sect. 2.

Appendix B. Spatial discretization

In this section, the spatial discretization is discussed for the proposed schemes. We first divide Ω in (73) into $n_r \times n_z$ cells, where n_r, n_z are the number of cells in the r and z directions. Each cell is characterized by $[(i-1)\Delta r, i\Delta r] \times [(j-1)\Delta z, j\Delta z]$ with the grid sizes $\Delta r = R/n_r$ and $\Delta z = L/n_z$. The cell center, and the centers of its top and right edges are indexed by (i, j), $(i, j+1/2)$, and $(i+1/2, j)$, respectively. Staggered grids are used: the axial velocity u_z and radial velocity u_r are evaluated at the edge center, while the order parameters ϕ and ψ, the chemical potentials μ_ϕ and μ_ψ, and the pressure p are solved at the cell center.

The grid values of variables (denoted by w below) at staggered grids are approximated by (second-order) linear interpolations. For instance, if w is solved at $(i, j+1/2)$, then

$$w_{i,j} = \frac{w_{i,j-\frac{1}{2}} + w_{i,j+\frac{1}{2}}}{2}, \qquad w_{i+\frac{1}{2},j+\frac{1}{2}} = \frac{w_{i,j+\frac{1}{2}} + w_{i+1,j+\frac{1}{2}}}{2}.$$

Similarly, for variable solved at $(i+1/2, j)$,

$$w_{i,j} = \frac{w_{i-\frac{1}{2},j} + w_{i+\frac{1}{2},j}}{2}, \qquad w_{i+\frac{1}{2},j+\frac{1}{2}} = \frac{w_{i+\frac{1}{2},j} + w_{i+\frac{1}{2},j+1}}{2}.$$

For variable solved at cell center (i, j), we can approximate the values at edge centers and corner point by

$$w_{i,j+\frac{1}{2}} = \frac{w_{i,j+1} + w_{i,j}}{2}, \qquad w_{i+\frac{1}{2},j} = \frac{w_{i+1,j} + w_{i,j}}{2}, \qquad w_{i+\frac{1}{2},j+\frac{1}{2}} = \frac{w_{i+1,j+1} + w_{i+1,j} + w_{i,j+1} + w_{i,j}}{4}.$$

The differential operators are discretized as

$$\nabla_h w_{i+\alpha,j+\nu} = \left(\frac{w_{i+\frac{1}{2}+\alpha,j+\nu} - w_{i-\frac{1}{2}+\alpha,j+\nu}}{\Delta r}, \frac{w_{i+\alpha,j+\frac{1}{2}+\nu} - w_{i+\alpha,j-\frac{1}{2}+\nu}}{\Delta z} \right),$$

$$\nabla_h \cdot \mathbf{u}_{i+\alpha,j+\nu} = \frac{r_{i+\frac{1}{2}+\alpha}(u_r)_{i+\frac{1}{2}+\alpha,j+\nu} - r_{i-\frac{1}{2}+\alpha}(u_r)_{i-\frac{1}{2}+\alpha,j+\nu}}{r_{i+\alpha}\Delta r} + \frac{(u_z)_{i+\alpha,j+\frac{1}{2}+\nu} - (u_z)_{i+\alpha,j-\frac{1}{2}+\nu}}{\Delta z},$$

$$\Delta_h w_{i+\alpha,j+\nu} = \frac{r_{i+\frac{1}{2}+\alpha}(w_{i+1+\alpha,j+\nu} - w_{i+\alpha,j+\nu}) - r_{i-\frac{1}{2}+\alpha}(w_{i+\alpha,j+\nu} - w_{i-1+\alpha,j+\nu})}{r_{i+\alpha}(\Delta r)^2} + \frac{w_{i+\alpha,j+1+\nu} - 2w_{i+\alpha,j+\nu} + w_{i+\alpha,j-1+\nu}}{(\Delta z)^2},$$

where $\alpha, \nu \in \{0, \frac{1}{2}\}$. Here, when $\alpha = \nu = 0$, it indicates that the differential operators are discretized at the cell center. Conversely, when $\alpha = \frac{1}{2}$ or $\nu = \frac{1}{2}$, it signifies discretization at the center of the edge. By substituting the differential operators in (27)–(40) and (58)–(72) with the corresponding discretized formulae, we can derive the fully discrete schemes in axisymmetric cylindrical coordinates.

In addition, the relaxation boundary condition is treated as follows. Using (9) and (13), we have the following relation

$$\text{Pe}_s \Delta \mu_\phi = -\text{Pe}_\phi L(\phi) \qquad \text{on } z = 0.$$

This equation is used in replacement of (13) in the implementation. For ϕ and μ_ϕ at $(i, -1/2)$ with $i = 0, \dots, n_r - 1$, we have

$$\text{Pe}_s [\Delta_h \mu_\phi^{n+1}]_{i,-\frac{1}{2}} = -\text{Pe}_\phi [L_\phi^{n+1}]_{i,-\frac{1}{2}},$$

where $\Delta_h \mu_\phi$ is evaluated on $(i, -1/2)$ using the boundary condition $\mu_{\phi_{i,-1}} = \mu_{\phi_{i,0}}$ and second-order extrapolation:

$$[\Delta_h \mu_\phi]_{i,-\frac{1}{2}} = \frac{r_{i+\frac{1}{2}}(\mu_{\phi_{i+1,0}} - \mu_{\phi_{i,0}}) - r_{i-\frac{1}{2}}(\mu_{\phi_{i,0}} - \mu_{\phi_{i-1,0}})}{r_i(\Delta r)^2} - \frac{(\mu_{\phi_{i,2}} - 5\mu_{\phi_{i,1}} + 4\mu_{\phi_{i,0}})}{2(\Delta z)^2}.$$

The remaining boundary conditions are discretized in the normal way, as with the bulk equations.

Appendix C. Extra numerical tests

Firstly, we perform several numerical experiments for uniform flow test in terms of Δt, h, Cn, Re, λ_ρ and λ_η, where $\text{Cn} = 2h$. Notably, the investigation focus on a fluid system in the absence of surfactants and the MCL. We choose that $\text{Pe}_\phi = 100$, $\text{We} = 100$, and set the following initial values

$$\phi(r, z, t=0) = \tanh\left(50\sqrt{2} \times (\sqrt{r^2 + (z-0.3)^2} - 0.25)\right), \qquad u_z(r, z, t=0) = 1, \qquad u_r(r, z, t=0) = 0,$$

and the boundary conditions

$$\partial_n \phi = 0, \qquad \partial_n \mu_\phi = 0, \qquad u_r = 0, \qquad u_z = 1 \qquad \text{on } \partial\Omega.$$
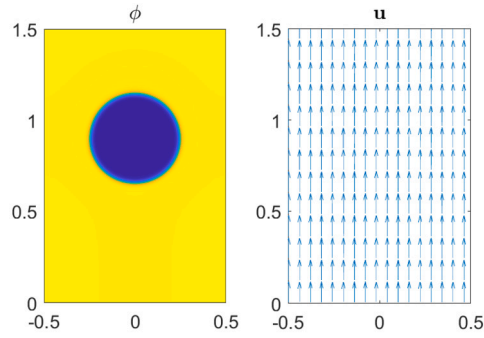
Fig. C.18. Uniform flow test ($\Delta t = 10^{-4}$, $h = 1/200$, Cn $= 1/100$, Re $= 100$, $\lambda_\rho = 1/50$, $\lambda_\eta = 1$). The numerical solutions for ϕ and **u** are computed using the first-order scheme at $t = 0.6$.
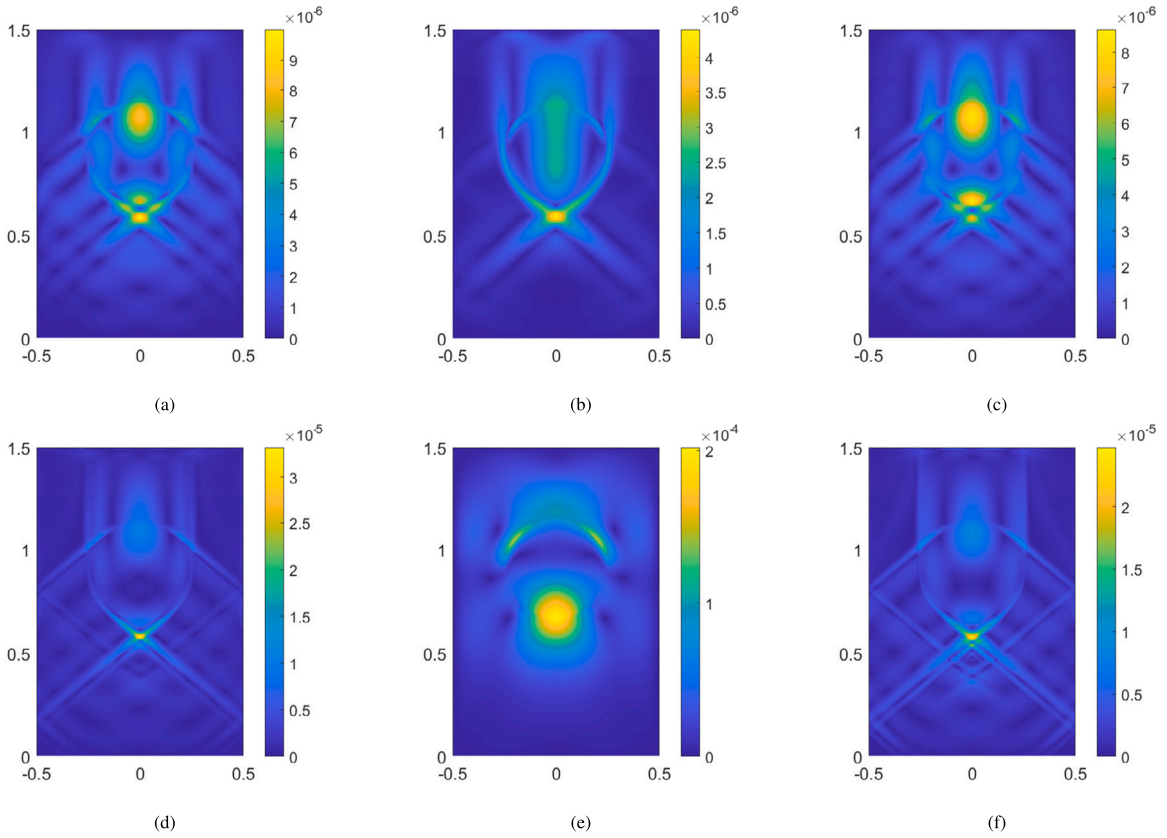

Fig. C.19. The difference $|\mathbf{u} - (0, 1)|$ obtained using the first-order scheme at $t = 0.6$. (a) $\Delta t = 10^{-4}$, $h = 1/200$, Cn $= 1/100$, Re $= 100$, $\lambda_\rho = 1$, $\lambda_\eta = 1$; (b) $\Delta t = 10^{-4}$, $h = 1/800$, Cn $= 1/400$, Re $= 100$, $\lambda_\rho = 1$, $\lambda_\eta = 1$; (c) $\Delta t = 2.5 \times 10^{-5}$, $h = 1/200$, Cn $= 1/100$, Re $= 100$, $\lambda_\rho = 1$, $\lambda_\eta = 1$; (d) $\Delta t = 10^{-4}$, $h = 1/200$, Cn $= 1/100$, Re $= 1000$, $\lambda_\rho = 1$, $\lambda_\eta = 1$; (e) $\Delta t = 10^{-4}$, $h = 1/200$, Cn $= 1/100$, Re $= 100$, $\lambda_\rho = 1/50$, $\lambda_\eta = 1$; (f) $\Delta t = 10^{-4}$, $h = 1/200$, Cn $= 1/100$, Re $= 100$, $\lambda_\rho = 1$, $\lambda_\eta = 1/50$.

In these numerical tests, we neglect the gravitational force and obtain the numerical solutions after a transient period. The results depicted in Fig. C.18 (at $t = 0.6$) illustrate the good performance of our first-order scheme in the context of uniform flow test. The uniform flow is clearly observed. Moreover, as shown in Figs. C.19, the deviations of the computed velocities from the uniform flow ($|\mathbf{u} - (0, 1)|$) are considerably small for various Δt, h, Cn, Re, λ_ρ, and λ_η settings.

We also perform extensive numerical experiments to quantify the error of $\nabla \cdot \mathbf{u}^{n+1}$ in terms of Δt, h, Cn, λ_ρ and λ_η, where Cn $= 2h$. We adopt the parameters and initial values as follows,

$$\mathrm{Pe}_\phi = 100, \quad \mathrm{Pe}_s = 0.002, \quad \mathrm{Pe}_\psi = 100, \quad \mathrm{Pi} = 0.1841, \quad \mathrm{Ex} = 1,$$

$$\mathrm{Re} = 200, \quad \mathrm{We} = 100, \quad \mathrm{L}_s = 0.0025, \quad \theta_s = 90°, \quad \lambda_{l_s} = 1,$$

Table C.3

The l_∞ errors and convergence rates for $\nabla \cdot \mathbf{u}^{n+1}$ are evaluated at $t = 0.4$ with different Δt, h and Cn.

1st-order scheme

| | | | $\lambda_\eta = 1$ | | | | $\lambda_\rho = 1$ | | | |
| | | | $\lambda_\rho = 0.5$ | | $\lambda_\rho = 0.01$ | | $\lambda_\eta = 0.5$ | | $\lambda_\eta = 0.01$ | |
Δt	h	Cn	error	order	error	order	error	order	error	order
1/200	1/100	1/50	3.16E−3	–	3.91E−3	–	2.18E−3	–	3.01E−3	–
1/400	1/200	1/100	1.93E−3	0.71	2.28E−3	0.78	1.26E−3	0.79	1.60E−3	0.91
1/800	1/400	1/200	1.09E−3	0.82	1.44E−3	0.66	7.19E−4	0.81	8.23E−4	0.96
1/1600	1/800	1/400	5.86E−4	0.90	8.22E−4	0.81	3.80E−4	0.92	4.47E−4	0.88

2nd-order scheme

| | | | $\lambda_\eta = 1$ | | | | $\lambda_\rho = 1$ | | | |
| | | | $\lambda_\rho = 0.5$ | | $\lambda_\rho = 0.01$ | | $\lambda_\eta = 0.5$ | | $\lambda_\eta = 0.01$ | |
Δt	h	Cn	error	order	error	order	error	order	error	order
1/200	1/100	1/50	9.16E−4	–	9.98E−4	–	8.12E−4	–	9.23E−4	–
1/400	1/200	1/100	3.93E−4	1.22	4.62E−4	1.11	3.61E−4	1.17	4.05E−4	1.19
1/800	1/400	1/200	1.78E−4	1.14	1.98E−4	1.22	1.44E−4	1.33	1.79E−4	1.18
1/1600	1/800	1/400	6.95E−5	1.36	9.86E−5	1.01	5.87E−5	1.29	7.30E−5	1.29

as well as the initial conditions:

$$\phi(r, z, t = 0) = \tanh\left(50\sqrt{2} \times (\sqrt{r^2 + (z - 0.25)^2} - 0.25)\right), \qquad \psi(r, z, t = 0) = 0.03,$$

$$u_z(r, z, t = 0) = -0.5 \times \left(1 - \tanh\left(50\sqrt{2} \times (\sqrt{r^2 + (z - 0.25)^2} - 0.25)\right)\right), \qquad u_r(r, z, t = 0) = 0.$$

As shown in Table C.3, the errors in $|\nabla \cdot \mathbf{u}^{n+1}|$ decay as Δt, h and Cn are all simultaneously refined for both the first-order and second-order schemes. The convergence rate for the second-order scheme is better than the first-order one.

References

[1] R.F. Probstein, Physicochemical Hydrodynamics: an Introduction, John Wiley & Sons, New York, 2005.

[2] C.D. Eggleton, T.-M. Tsai, K.J. Stebe, Tip streaming from a drop in the presence of surfactants, Phys. Rev. Lett. 87 (2001) 048302.

[3] A.B. Branger, D.M. Eckmann, Accelerated arteriolar gas embolism reabsorption by an exogenous surfactant, Anesthesiology 96 (2002) 971–979.

[4] J.-C. Baret, Surfactants in droplet-based microfluidics, Lab Chip 12 (2012) 422–433.

[5] S. Kommeren, M.J. Coenen, T.M. Eggenhuisen, T.W. Slaats, H. Gorter, P. Groen, Combining solvents and surfactants for inkjet printing pedot: Pss on p3ht/pcbm in organic solar cells, Org. Electron. 61 (2018) 282–288.

[6] H. Garcke, K.F. Lam, B. Stinner, Diffuse interface modelling of soluble surfactants in two-phase flow, Commun. Math. Sci. 12 (2014) 1475–1522.

[7] H.A. Stone, A simple derivation of the time-dependent convective-diffusion equation for surfactant transport along a deforming interface, Phys. Fluids A 2 (1990) 111–112.

[8] H. Wong, D. Rumschitzki, C. Maldarelli, On the surfactant mass balance at a deforming fluid interface, Phys. Fluids 8 (1996) 3203–3204.

[9] M. Muradoglu, G. Tryggvason, A front-tracking method for computation of interfacial flows with soluble surfactants, J. Comput. Phys. 227 (2008) 2238–2262.

[10] C. Cleret de Langavant, A. Guittet, M. Theillard, F. Temprano-Coleto, F. Gibou, Level-set simulations of soluble surfactant driven flows, J. Comput. Phys. 348 (2017) 271–297.

[11] A.J. James, J. Lowengrub, A surfactant-conserving volume-of-fluid method for interfacial flows with insoluble surfactant, J. Comput. Phys. 201 (2004) 685–722.

[12] K.-Y. Chen, M.-C. Lai, A conservative scheme for solving coupled surface-bulk convection-diffusion equations with an application to interfacial flows with soluble surfactant, J. Comput. Phys. 257 (2014) 1–18.

[13] H. Liu, Y. Zhang, Phase-field modeling droplet dynamics with soluble surfactants, J. Comput. Phys. 229 (2010) 9166–9187.

[14] G. Zhu, J. Kou, S. Sun, J. Yao, A. Li, Numerical approximation of a phase-field surfactant model with fluid flow, J. Sci. Comput. 80 (2019) 223–247.

[15] H. Liu, J. Zhang, Y. Ba, N. Wang, L. Wu, Modelling a surfactant-covered droplet on a solid surface in three-dimensional shear flow, J. Fluid Mech. 897 (2020) A33, 31.

[16] M. Laradji, H. Guo, M. Grant, M.J. Zuckermann, The effect of surfactants on the dynamics of phase separation, J. Phys. Condens. Matter 4 (1992) 6715.

[17] C.-H. Teng, I.-L. Chern, M.-C. Lai, Simulating binary fluid-surfactant dynamics by a phase field model, Discrete Contin. Dyn. Syst., Ser. B 17 (2012) 1289–1307.

[18] S. Gu, H. Zhang, Z. Zhang, An energy-stable finite-difference scheme for the binary fluid-surfactant system, J. Comput. Phys. 270 (2014) 416–431.

[19] J. Yang, J. Kim, An improved scalar auxiliary variable (SAV) approach for the phase-field surfactant model, Appl. Math. Model. 90 (2021) 11–29.

[20] X. Yang, A novel fully-decoupled, second-order and energy stable numerical scheme of the conserved Allen-Cahn type flow-coupled binary surfactant model, Comput. Methods Appl. Mech. Eng. 373 (2021) 113502, 26.

[21] R. van der Sman, S. van der Graaf, Diffuse interface model of surfactant adsorption onto flat and droplet interfaces, Rheol. Acta 46 (2006) 3–11.

[22] S. Engblom, M. Do-Quang, G. Amberg, A.-K. Tornberg, On diffuse interface modeling and simulation of surfactants in two-phase fluid flow, Commun. Comput. Phys. 14 (2013) 879–915.

[23] J. Shen, J. Xu, J. Yang, A new class of efficient and robust energy stable schemes for gradient flows, SIAM Rev. 61 (2019) 474–506.

[24] D.J. Eyre, Unconditionally gradient stable time marching the Cahn-Hilliard equation, in: Computational and Mathematical Models of Microstructural Evolution, San Francisco, CA, 1998, in: Mater. Res. Soc. Sympos. Proc., vol. 529, MRS, Warrendale, PA, San Francisco, 1998, pp. 39–46.

[25] L.Q. Chen, J. Shen, Applications of semi-implicit Fourier-spectral method to phase field equations, Comput. Phys. Commun. 108 (1998) 147–158.

[26] F. Guillén-González, G. Tierra, On linear schemes for a Cahn-Hilliard diffuse interface model, J. Comput. Phys. 234 (2013) 140–171.

[27] J. Zhao, Q. Wang, X. Yang, Numerical approximations for a phase field dendritic crystal growth model based on the invariant energy quadratization approach, Int. J. Numer. Methods Eng. 110 (2017) 279–300.

[28] J. Shen, J. Xu, J. Yang, The scalar auxiliary variable (SAV) approach for gradient flows, J. Comput. Phys. 353 (2018) 407–416.

[29] C. Chen, K. Pan, X. Yang, Numerical approximations of a hydro-dynamically coupled phase-field model for binary mixture of passive/active nematic liquid crystals and viscous fluids, Appl. Numer. Math. 158 (2020) 1–21.

[30] X. Yang, L. Ju, Linear and unconditionally energy stable schemes for the binary fluid-surfactant phase field model, Comput. Methods Appl. Mech. Eng. 318 (2017) 1005–1029.

[31] Y. Qin, Z. Xu, H. Zhang, Z. Zhang, Fully decoupled, linear and unconditionally energy stable schemes for the binary fluid-surfactant model, Commun. Comput. Phys. 28 (2020) 1389–1414.

[32] X. Yang, H. Yu, Efficient second order unconditionally stable schemes for a phase field moving contact line model using an invariant energy quadratization approach, SIAM J. Sci. Comput. 40 (2018) B889–B914.

[33] F. Huang, J. Shen, Z. Yang, A highly efficient and accurate new scalar auxiliary variable approach for gradient flows, SIAM J. Sci. Comput. 42 (2020) A2514–A2536.

[34] Q. Cheng, J. Shen, Global constraints preserving scalar auxiliary variable schemes for gradient flows, SIAM J. Sci. Comput. 42 (2020) A2489–A2513.

[35] J. Xu, Y. Li, S. Wu, A. Bousquet, On the stability and accuracy of partially and fully implicit schemes for phase field modeling, Comput. Methods Appl. Mech. Eng. 345 (2019) 826–853.

[36] Q. Du, L. Ju, X. Li, Z. Qiao, Maximum bound principles for a class of semilinear parabolic equations and exponential time-differencing schemes, SIAM Rev. 63 (2021) 317–359.

[37] T. Young, An essay on the cohesion of fluids, Philos. Trans. R. Soc. Lond. 95 (1805) 65–87.

[38] D. Jacqmin, Contact-line dynamics of a diffuse fluid interface, J. Fluid Mech. 402 (2000) 57–88.

[39] T. Qian, X.-P. Wang, P. Sheng, Molecular scale contact line hydrodynamics of immiscible flows, Phys. Rev. E 68 (2003) 016306.

[40] W. Ren, W. E, Boundary conditions for the moving contact line problem, Phys. Fluids 19 (2007) 022101.

[41] J. Eggers, Hydrodynamic theory of forced dewetting, Phys. Rev. Lett. 93 (2004) 094502.

[42] J. De Coninck, T.D. Blake, Wetting and molecular dynamics simulations of simple liquids, Annu. Rev. Mater. Res. 38 (2008) 1–22.

[43] P. Yue, C. Zhou, J.J. Feng, Sharp-interface limit of the Cahn-Hilliard model for moving contact lines, J. Fluid Mech. 645 (2010) 279–294.

[44] Y. Sui, H. Ding, P.D.M. Spelt, Numerical simulations of flows with moving contact lines, Annu. Rev. Fluid Mech. 46 (2014) 97–119.

[45] M.-C. Lai, Y.H. Tseng, H. Huang, Numerical simulation of moving contact lines with surfactant by immersed boundary method, Commun. Comput. Phys. 8 (2010) 735–757.

[46] J.-J. Xu, W. Ren, A level-set method for two-phase flows with moving contact line and insoluble surfactant, J. Comput. Phys. 263 (2014) 71–90.

[47] Z. Zhang, S. Xu, W. Ren, Derivation of a continuum model and the energy law for moving contact lines with insoluble surfactants, Phys. Fluids 26 (2014) 062103.

[48] Q. Zhao, W. Ren, Z. Zhang, A thermodynamically consistent model and its conservative numerical approximation for moving contact lines with soluble surfactants, Comput. Methods Appl. Mech. Eng. 385 (2021) 114033, 28.

[49] G. Zhu, J. Kou, B. Yao, Y.-s. Wu, J. Yao, S. Sun, Thermodynamically consistent modelling of two-phase flows with moving contact line and soluble surfactants, J. Fluid Mech. 879 (2019) 327–359.

[50] G. Zhu, J. Kou, J. Yao, A. Li, S. Sun, A phase-field moving contact line model with soluble surfactants, J. Comput. Phys. 405 (2020) 109170, 29.

[51] C. Wang, Y. Guo, Z. Zhang, Unconditionally energy stable and bound-preserving schemes for phase-field surfactant model with moving contact lines, J. Sci. Comput. 92 (2022) 20, 29.

[52] F. Afolabi, S.M. Mahmood, N. Yekeen, S. Akbari, H. Sharifigaliuk, Polymeric surfactants for enhanced oil recovery: a review of recent progress, J. Pet. Sci. Eng. 208 (2022) 109358.

[53] P.-G. de Gennes, F. Brochard-Wyart, D. Quéré, et al., Capillarity and Wetting Phenomena: Drops, Bubbles, Pearls, Waves, vol. 315, Springer, New York, 2004.

[54] K.P. Gatne, M.A. Jog, R.M. Manglik, Surfactant-induced modification of low Weber number droplet impact dynamics, Langmuir 25 (2009) 8122–8130.

[55] K.-L. Pan, Y.-H. Tseng, J.-C. Chen, K.-L. Huang, C.-H. Wang, M.-C. Lai, Controlling droplet bouncing and coalescence with surfactant, J. Fluid Mech. 799 (2016) 603–636.

[56] T. Qian, X.-P. Wang, P. Sheng, A variational approach to moving contact line hydrodynamics, J. Fluid Mech. 564 (2006) 333–360.

[57] H. Yu, X. Yang, Numerical approximations for a phase-field moving contact line model with variable densities and viscosities, J. Comput. Phys. 334 (2017) 665–686.

[58] D. Richard, C. Clanet, D. Quéré, Contact time of a bouncing drop, Nature 417 (2002) 811.

[59] R. Rioboo, M. Marengo, C. Tropea, Time evolution of liquid drop impact onto solid, dry surfaces, Exp. Fluids 33 (2002) 112–124.

[60] Y. Renardy, S. Popinet, L. Duchemin, M. Renardy, S. Zaleski, C. Josserand, M. Drumright-Clarke, D. Richard, C. Clanet, D. Quéré, Pyramidal and toroidal water drops after impact on a solid surface, J. Fluid Mech. 484 (2003) 69–83.

[61] Q. Zhang, T.-Z. Qian, X.-P. Wang, Phase field simulation of a droplet impacting a solid surface, Phys. Fluids 28 (2016) 022103.

[62] X. Xu, Y. Di, H. Yu, Sharp-interface limits of a phase-field model with a generalized Navier slip boundary condition for moving contact lines, J. Fluid Mech. 849 (2018) 805–833.

[63] H. Abels, H. Garcke, G. Grün, Thermodynamically consistent, frame indifferent diffuse interface models for incompressible two-phase flows with different densities, Math. Models Methods Appl. Sci. 22 (2012) 1150013, 40.

[64] J. Shen, X. Yang, Numerical approximations of Allen-Cahn and Cahn-Hilliard equations, Discrete Contin. Dyn. Syst. 28 (2010) 1669–1691.

[65] M. Gao, X.-P. Wang, An efficient scheme for a phase field model for the moving contact line problem with variable density and viscosity, J. Comput. Phys. 272 (2014) 704–718.

[66] Y. Gong, Q. Hong, Q. Wang, Supplementary variable method for thermodynamically consistent partial differential equations, Comput. Methods Appl. Mech. Eng. 381 (2021) 113746, 19.

[67] D. Li, C. Quan, T. Tang, Stability and convergence analysis for the implicit-explicit method to the Cahn-Hilliard equation, Math. Comput. 91 (2022) 785–809.

[68] D. Li, Why large time-stepping methods for the Cahn-Hilliard equation is stable, Math. Comput. 91 (2022) 2501–2515.

[69] M.I.M. Copetti, C.M. Elliott, Numerical analysis of the Cahn-Hilliard equation with a logarithmic free energy, Numer. Math. 63 (1992) 39–65.

[70] J. Shen, X. Yang, Decoupled, energy stable schemes for phase-field models of two-phase incompressible flows, SIAM J. Numer. Anal. 53 (2015) 279–296.

[71] X. Yang, On a novel fully decoupled, second-order accurate energy stable numerical scheme for a binary fluid-surfactant phase-field model, SIAM J. Sci. Comput. 43 (2021) B479–B507.

[72] J. Shen, T. Tang, Spectral and High-Order Methods with Applications, Mathematics Monograph Series, vol. 3, Science Press Beijing, Beijing, 2006.

[73] X.-D. Liu, S. Osher, T. Chan, Weighted essentially non-oscillatory schemes, J. Comput. Phys. 115 (1994) 200–212.

[74] J. Lowengrub, L. Truskinovsky, Quasi-incompressible Cahn-Hilliard fluids and topological transitions, Proc. R. Soc. A, Math. Phys. Eng. Sci. 454 (1998) 2617–2654.

[75] Z. Guo, P. Lin, J. Lowengrub, S.M. Wise, Mass conservative and energy stable finite difference methods for the quasi-incompressible Navier-Stokes-Cahn-Hilliard system: primitive variable and projection-type schemes, Comput. Methods Appl. Mech. Eng. 326 (2017) 144–174.